ADVANCED MATERIALS
www.advmat.de

Quinoidal Semiconductor Nanoparticles for NIR-II Photoacoustic Imaging and Photoimmunotherapy of Cancer

*Gaoli Niu, Guangkun Song, Yong Kang, Yanhong Zhai, Yueyue Fan, Jiamin Ye, Ruiyan Li, Runtan Li, Yanwei Zhang, Hong Wang, Yongsheng Chen, and Xiaoyuan Ji**

Photoagents with ultra-high near-infrared II (NIR-II) light energy conversion efficiency hold great promise in tumor phototherapy due to their ability to penetrate deeper tissues and minimize damage to surrounding healthy cells. However, the development of NIR-II photoagents remain challenging. In this study, an all-fused-ring quinoidal acceptor-donor-acceptor (A-D-A) molecule, SKCN, with a BTP core is synthesized, and nanoparticles named FA-SNPs are prepared. The unique quinoidal structure enhances π-electron delocalization and bond length uniformity, significantly reducing the bandgap of SKCN, resulting in strong NIR-II absorption, a high molar extinction coefficient, and a photothermal conversion efficiency of 75.14%. Enhanced molecular rigidity also facilitates efficient energy transfer to oxygen, boosting reactive oxygen species generation. By incorporating the immunomodulator R848, FA-SRNPs nanoparticles are further developed, effectively modulating the tumor immune microenvironment by reducing Tregs and M-MDSCs infiltration, promoting dendritic cell maturation, M1 macrophage polarization, and activating CD8+ T cells and NK cells. Comprehensive studies using orthotopic ovarian cancer models demonstrated strong tumor targeting, photoacoustic imaging capabilities, and significant tumor suppression and metastasis inhibition, and also showing excellent therapeutic efficacy in an orthotopic breast cancer model. This study provides strong evidence for the potential application of quinoidal A-D-A molecules in cancer photoimmunotherapy.

1. Introduction

Ovarian cancer remains one of the leading causes of cancer-related mortality among women worldwide.[1] Due to the absence of effective early diagnostic methods, ≈70% of ovarian cancer cases are identified at an advanced stage, often accompanied by extensive metastasis and significant ascites,[2] resulting in poor treatment outcomes and prognosis.[3] As a result, the development of novel therapeutic strategies and early detection methods is essential to improving the survival rates of ovarian cancer patients.[4] In recent years, photothermal therapy (PTT) and photodynamic therapy (PDT) have garnered attention as promising modalities for cancer treatment.[5] By utilizing near-infrared (NIR) light excitation, PTT-PDT agent can efficiently absorb light energy, converting it into heat or generating reactive oxygen species (ROS), which subsequently induces tumor cell death.[6] However, traditional organic materials are limited by their broad bandgaps, low light absorption, and energy conversion efficiency, as well as insufficient deep tissue penetration.[7] These factors restrict their effectiveness in treating deep-seated tumors, such as ovarian cancer. Consequently, the development of innovative photosensitizing materials tailored for deep-seated tumors, capable of enhancing photothermal conversion efficiency and improving the efficacy of photodynamic therapy, is imperative.

With a growing understanding of structure–performance relationships, various molecular design strategies have emerged to effectively modulate energy levels in organic semiconductors. In recent years, n-type small-molecule organic semiconductors

G. Niu, Y. Kang, Y. Fan, J. Ye, R. Li, R. Li, X. Ji
Academy of Medical Engineering and Translational Medicine
Medical College
Tianjin University
Tianjin 300072, China
E-mail: jixiaoyuan@tju.edu.cn
G. Niu, Y. Zhai, H. Wang
The First Affiliated Hospital of Henan Polytechnic University
Jiaozuo 454000, China
G. Song, Y. Chen
State Key Laboratory and Institute of Elemento-Organic Chemistry
The Centre of Nanoscale Science and Technology and Key Laboratory of Functional Polymer Materials
Renewable Energy Conversion and Storage Center (RECAST)
Tianjin Key Laboratory of Functional Polymer Materials
College of Chemistry
Nankai University
Tianjin 300071, China
Y. Zhang
Xiyingmen Subdistrict Community Health Service Center
Xiqing District, Tianjin 300072, China
X. Ji
Medical College
Linyi University
Linyi 276000, China

The ORCID identification number(s) for the author(s) of this article can be found under https://doi.org/10.1002/adma.202415189

DOI: 10.1002/adma.202415189

with an acceptor-donor-acceptor (A-D-A) framework, commonly referred to as nonfullerene acceptors (NFAs),[8] have garnered substantial success. These NFAs demonstrate optimal energy levels, minimal band tail states, high crystallinity, and low exciton binding energy,[9] positioning them as a focal point of research in the development of organic solar cells.[10] Notably, the introduction of Y6 has driven the power conversion efficiency (PCE) of organic photovoltaics (OPVs) beyond 20%.[11] However, the inherent bandgaps of NFAs limit their light absorption wavelength to below 1000 nm.[12] To enhance NIR-II light absorption in organic semiconductors, which is crucial for achieving deeper tissue penetration in applications such as PTT for deep-seated tumors, reducing the optical bandgap of NFAs can be accomplished by modulating intramolecular charge transfer (ICT) effects or incorporating quinoidal structures.[13] The introduction of quinoidal units can stabilize the quinoidal form of the aromatic rings, compensate for the loss of aromaticity, and lead to greater delocalization of the p-electron system, resulting in uniform bond lengths and a reduced bandgap.[14] The introduction of quinoidal structures into organic materials enhances their PTT and PDT effects through several key mechanisms. First, quinoidal structures reduce the bandgap of organic materials, enabling absorption of longer wavelengths in the NIR region, particularly in the NIR-II range, which provides deeper tissue penetration critical for effective PTT.[15] The reduced bandgap also increases the PTT-PDT agent's light absorption efficiency, facilitating greater heat generation under irradiation, thereby enhancing the photothermal effect. Second, quinoidal structures promote π-electron delocalization, improving the efficiency of photoinduced electron transfer.[16] This leads to increased ROS production in PDT, a key mechanism for inducing oxidative stress and tumor cell destruction. Third, all-fused-ring struction increases the rigidity of the molecule and reduces the number of reaction sites of PTT-PDT,[17] ensuring prolonged activity in biological environments and more effective accumulation at tumor sites, reducing premature degradation. Lastly, the introduction of quinoidal structures extends the excited-state lifetime of photosensitizers, allowing for more efficient chemical reactions with molecular oxygen,[18] thus boosting ROS generation in PDT and improving heat conversion in PTT. These mechanisms collectively enhance the therapeutic efficacy of quinoidal-structured organic materials in both PTT and PDT, making them more effective for the treatment of deep-seated tumors.

Despite the development of narrow bandgap organic molecules capable of absorbing NIR-II light for PTT and PDT in deep-seated tumors, addressing the high metastatic potential of ovarian cancer remains a significant challenge.[19] Phototherapy, as a primary method to induce immunogenic cell death (ICD) in tumor cells,[20] triggers the release of damage-associated molecular patterns (DAMPs) such as calreticulin (CRT), high mobility group box 1 (HMGB1), and tumor-associated antigens (TAAs), thereby initiating specific antitumor immune responses.[21] However, the immune response elicited by phototherapy alone may be insufficient to fully eradicate tumors. Therefore, the combination of phototherapy with immunomodulatory agents, known as photoimmunotherapy (PIT), has emerged as a more potent therapeutic strategy. R848, a powerful Toll-like receptor (TLR) 7/8 agonist,[22] can enhance dendritic cell (DC) maturation, promote antigen presentation, modulate the tumor microenvironment, decrease the population of immunosuppressive cells such as tumor-associated macrophages (TAMs), regulatory T cells (Tregs) and myeloid-derived suppressor cells (M-MDSCs), induce M1 macrophage polarization, and activate $CD8^+$ cytotoxic T cells, thereby significantly amplifying antitumor effects.[23] However, systemic administration of R848 via intravenous injection may cause adverse effects such as fever, appetite loss, and fatigue.[23b,24] Additionally, the intravenous administration of photosensitizers presents challenges related to tumor-specific accumulation, and their activation in non-tumor tissues can result in collateral damage to healthy tissues.

To enhance the targeting and controlled release of PTT-PDT agent and R848 at tumor sites, organic molecules and therapeutic agents can be formulated into nanoparticles. Folate (FA) receptors, which are highly expressed in many ovarian cancer subtypes, serve as promising targets for drug delivery. Mirvetuximab soravtansine, an antibody-drug conjugate targeting folate receptor alpha (FRα), has been approved for the treatment of platinum-resistant ovarian cancer.[25] Additionally, clinical studies are investigating the use of FRα-targeted fluorescent probes for tumor-specific imaging during ovarian cancer surgery.[26] To further improve drug release efficiency at the tumor site, the unique characteristics of the tumor microenvironment, such as elevated glutathione (GSH) levels (≈10–30 mM), can be exploited.[27] The incorporation of FA-modified nanoparticles significantly enhances their targeting to ovarian cancer cells. Furthermore, the introduction of disulfide bonds into the nanoparticle structure enables their cleavage in the high-GSH environment, promoting the release of encapsulated organic molecules and R848.[28] This approach not only increases the therapeutic efficacy but also minimizes systemic side effects by ensuring selective drug release within the tumor microenvironment. Additionally, photoacoustic imaging (PAI), an emerging imaging modality that combines the high contrast of optical imaging with the deep tissue penetration of ultrasound, holds significant promise for early tumor detection and treatment evaluation.[29] Particularly for deep-seated and occult tumors such as ovarian cancer, photoacoustic imaging has the potential to greatly enhance early diagnostic accuracy. As a result, the design of organic small molecules capable of generating both NIR-II photothermal and photodynamic effects, while simultaneously supporting photoacoustic imaging, is critical for the diagnosis and treatment of ovarian cancer.

To meet the aforementioned requirements, this study designed and developed an ultra-low bandgap n-type organic molecule, SKCN, featuring a quinonized BTP (Y6) core structure (**Figure 1A**). Compared to the traditional reference molecule Y6 (BTP-4F),[30] SKCN exhibited a significantly expanded absorption range, extending into the NIR-II region. This spectral expansion is primarily attributed to bandgap narrowing and enhanced π-electron delocalization induced by the quinoidal structure, thereby significantly enhancing the efficacy of PTT and PDT. To further improve the efficacy of photothermal immunotherapy (PIT), enhance tumor targeting, and achieve controlled drug release within the tumor microenvironment, SKCN was formulated with the immunomodulator R848 into nanoparticles, termed FA-SNPs and FA-SRNPs, respectively, using three different types of polyethylene glycol (PEG) coatings (Figure 1B). To closely resemble the clinical characteristics of ovarian cancer, an orthotopic ovarian cancer mouse model was established.

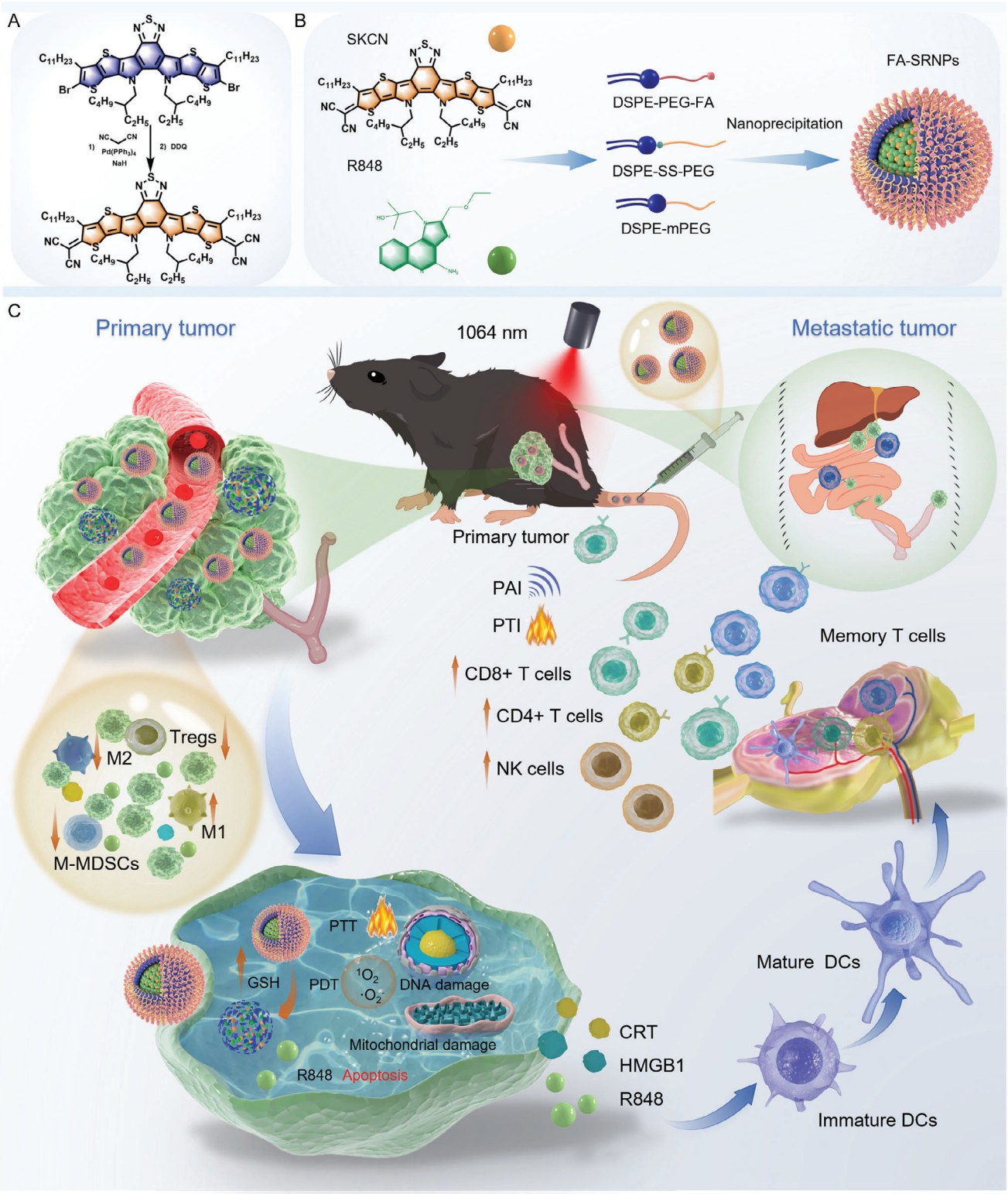

Figure 1. Schematic illustration of NIR-II photoimmunotherapy and photoacoustic imaging for orthotopic ovarian cancer using SKCN-based nanoparticles. A) Synthesis of the SKCN molecule. B) Preparation of FA-SRNPs by encapsulating SKCN and R848 with three different PEGs. C) Photoacoustic imaging of the PA_{1064} channel and 1064 nm laser-triggered photoimmunotherapy targeting primary and metastatic tumors.

The experimental results demonstrated that these nanoparticles exhibited excellent tumor targeting and accumulation capabilities and achieved high-quality photoacoustic imaging through the PA1064 channel. Additionally, PIT treatment not only effectively eradicated the primary tumor but also significantly inhibited peritoneal metastasis and ascites formation (Figure 1C). Furthermore, their remarkable therapeutic efficacy was also validated in an orthotopic breast cancer model. This study provides strong support for the application of this novel quinoidal organic molecule in NIR-II photothermal immunotherapy and photoacoustic imaging, revealing its great potential for precision tumor treatment.

2. Results and Discussion

2.1. Preparation and Characterization of SKCN, FA-SNPs, and FA-SRNPs

The quinoidal molecule SKCN was synthesized by 2, 10 – dibromo – 12, 13 – bis (2-ethylhexyl) – 3, 9 – diundecyl – 12, 13 – dihydro – [1,2,5] thiadiazolo [3,4-e] thieno [2′‴,3′‴:4′,5′] thieno [2′,3′:4,5] pyrrolo [3,2-g] thieno [2′,3′:4,5] thieno [3,2-b] indole coupling with malononitrile and then oxidized by DDQ (Figure 1A; Figures S1–S3, Supporting Information). The SKCN molecule features a quinoidal BTP core, structurally analogous to BTP-4F (Y6) (**Figure** 2A). The $O_{H/L}$ values for Y6 and SKCN were calculated to be 0.6967 and 0.8153 a.u., respectively (Figure 2B), where a higher $O_{H/L}$ value indicates greater electron localization, enhancing light absorption capabilities.[31] Cyclic voltammetry (CV) measurements were performed to further investigate the frontier molecular orbital energy levels of SKCN and Y6. The highest occupied molecular orbital (HOMO)/lowest unoccupied molecular orbital (LUMO) determined by CV were −5.26 eV/−4.38 eV for SKCN and -5.68 eV/-3.87 eV for Y6, aligning with the DFT results (Figure 2D; Figure S4, Supporting Information). Density Functional Theory (DFT) calculations estimated the HOMO and LUMO energy levels of SKCN at −5.33 eV and −4.23 eV, respectively, with a bandgap (Eg) of 1.10 eV (Figure 2E). In contrast, Y6 exhibited HOMO and LUMO levels of −5.62 eV and −3.58 eV, respectively, with a bandgap of 2.04 eV (Figure 2F). Additionally, SKCN's lower energy levels compared to Y6 enhance its light energy absorption efficiency, facilitating the conversion of absorbed light into heat through nonradiative pathways (Figure 2C). The molar extinction coefficient of SKCN was calculated to be $\epsilon = 8.634 \times 10^4\ m^{-1}\ cm^{-1}$, indicating strong light absorption (Figures S5 and S6, Supporting Information). SKCN is highly soluble in organic solvents, and to improve its biocompatibility and colloidal stability for vivo applications, it was formulated into nanoparticles, termed FA-SNPs, using a nanoprecipitation method as described in the literature. Fluorescence spectroscopy revealed that SKCN exhibits no fluorescence in solution or nanoparticle form (Figure S7, Supporting Information), consistent with the energy gap law from the Jablonski diagram. A narrower bandgap increases the probability of nonradiative transitions (heat release) while reducing radiative transitions (fluorescence), thus favoring heat generation over fluorescence emission[32] (Figure 2C). UV–vis–NIR absorption spectra were obtained for SKCN in solution, solid (film), and nanoparticle forms. In tetrahydrofuran (THF) solution, SKCN displayed a maximum absorption peak at 921 nm, with an absorption cutoff ≈1150 nm. In comparison, the reference molecule BTP-4F, which lacks a quinoidal structure, showed a cutoff at 800 nm. FA-SNPs exhibited a maximum absorption peak at 941 nm, with a cutoff near 1200 nm. The solid-state SKCN film demonstrated a redshifted maximum absorption peak at 1050 nm, with a cutoff extending beyond 1400 nm (Figure 2G). Compared to its solution state, SKCN, when formulated as nanoparticles, exhibits broader and stronger light absorption with a redshifted maximum absorption peak, significantly enhancing light penetration depth and improving its effectiveness in phototherapy for deep-seated tumors. This performance is closely related to the molecular structure of SKCN. Through the D–A alternating strategy, SKCN significantly enhances ICT, effectively reduces the energy gap, and achieves strong red-shifted absorption in the NIR-II region.[33] The quinone-based structure minimizes bond length alternation and enhances π-electron delocalization, further improve its NIR-II absorption performance.[34] Furthermore, hemolysis testing revealed an exceptionally low hemolysis rate for red blood cells co-incubated with FA-SNPs, indicating excellent hemocompatibility and suggesting that FA-SNPs are preliminarily suitable for intravenous administration (Figure S8, Supporting Information).

FA-SRNPs were synthesized via the nanoprecipitation method,[35] incorporating R848 and SKCN as core components, and utilizing three distinct PEG derivatives: 1,2-Distearoyl-sn-glycero-3-phosphoethanolamine-N-methoxy(polyethylene glycol) (DSPE-mPEG), DSPE-SS-PEG, and DSPE-PEG-FA. DSPE-mPEG significantly enhanced the stability, dispersibility, and biocompatibility of the nanoparticles, thereby extending their circulation time.[36] The elevated glutathione (GSH) concentration in metabolically active tumor cells triggers the reduction of disulfide bonds in DSPE-SS-PEG, leading to drug release specifically at the tumor site and minimizing the systemic side effects of R848. Folate receptor alpha (FR-α), a GPI-anchored membrane protein, is selectively overexpressed in over 90% of ovarian cancers, with expression levels 100–300 times higher than those in normal tissues.[37] Consequently, PEG derivatives containing both disulfide bonds and FA can significantly enhance the accumulation of photosensitizers and R848 in tumor tissues, improving intracellular delivery efficiency and reducing toxicity to normal tissues, ultimately increasing therapeutic efficacy. Transmission electron microscopy (TEM) analysis revealed that both FA-SNPs and FA-SRNPs exhibited uniform spherical morphologies with diameters of ≈100 nm, with FA-SRNPs being slightly larger than SNPs (Figure 2H). Zeta potential measurements showed that the nanoparticles had negatively charged surfaces, with FA-SNPs having a maximum negative charge of −26.5 mV and FA-SRNPs exhibiting −18.9 mV (Figure 2I). The hydrodynamic diameters of FA-SNPs and FA-SRNPs were measured to be 104 and 123 nm, respectively (Figure 2J). Additionally, when FA-SRNPs (25 μg mL^{-1}) were dissolved in Dulbecco's Modified Eagle Medium (DMEM), Phosphate-Buffered Saline (PBS), or water, no significant changes in morphology or hydrodynamic size were observed over a two-week period (Figure S9, Supporting Information), demonstrating the excellent stability of both FA-SNPs and FA-SRNPs. Their appropriate size and surface charge profile support prolonged circulation time in the bloodstream and enhanced

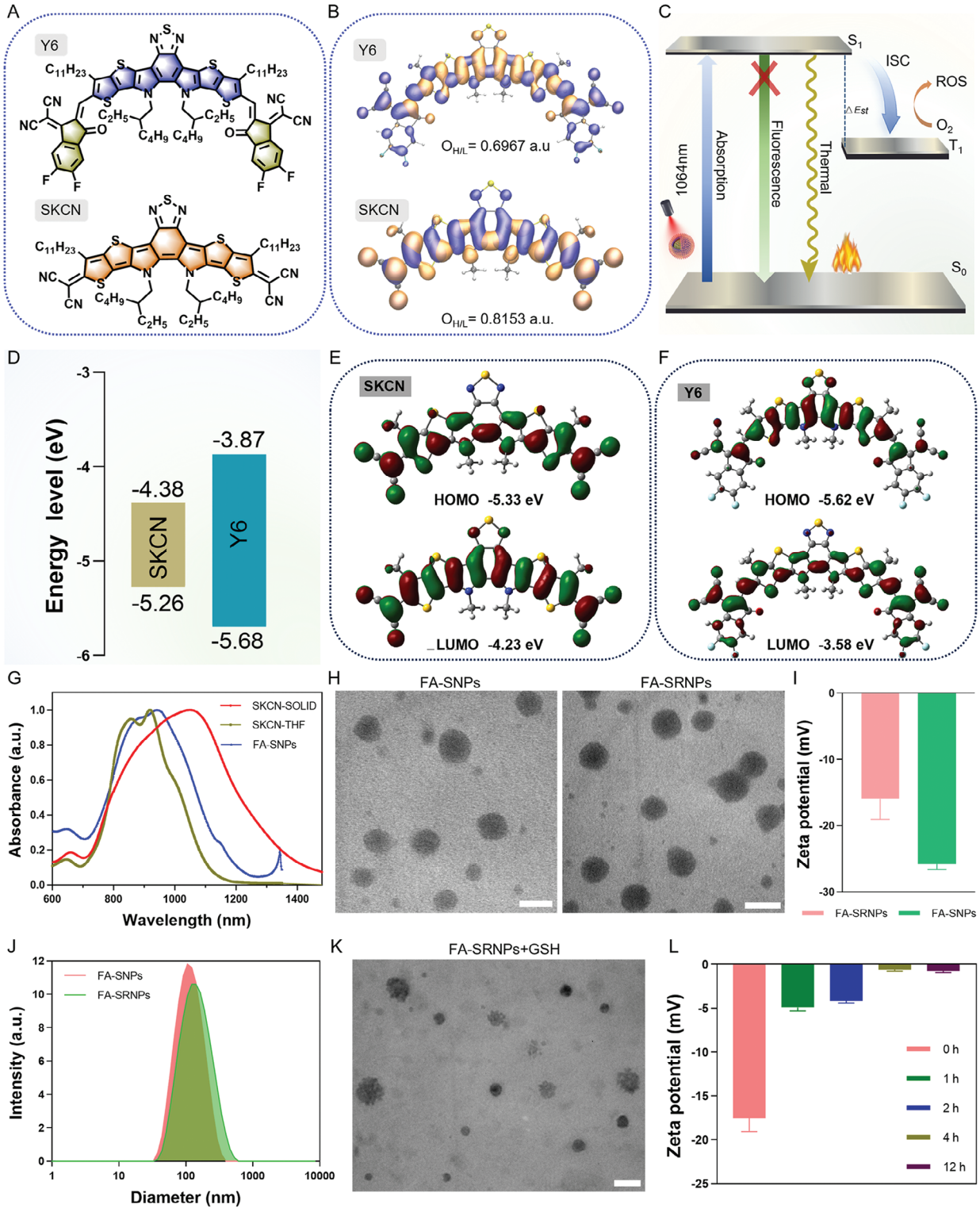

Figure 2. Comparison of SKCN and Y6, along with the characterization of SKCN and nanoparticles. A) Molecular structure comparison of SKCN and Y6. B) TD-DFT calculated molecular orbitals and energy diagrams at the B3LYP/6-31G(d) level. $O_{H/L}$ represents overlap integral between HOMO and LUMO. (HOMO: orange, LUMO: blue). C) Simulated Jablonski diagram. D) Energy level diagram of SKCN and Y6 derived from the electrochemical cyclic voltammetry. Molecular structures and theoretical density distribution for the frontier molecular orbits of HOMO and LUMO for SKCN and E) and Y6 F), calculated using DFT method. G) UV–vis absorption spectra of SKCN in different states. H) TEM images of FA-SNPs and FA-SRNPs. Scale bar = 100 μm. I) Zeta potential of FA-SNPs and FA-SRNPs. J) Particle size distributions of FA-SNPs and FA-SRNPs. K) TEM images of FA-SRNPs after incubation with GSH. Scale bar = 100 μm. L) Zeta potential changes of FA-SRNPs over time after incubation with GSH.

retention within tumor tissues. GSH concentration in the tumor microenvironment is significantly higher than that in the extracellular matrix (≈2–10 μM) and red blood cells (0.4–3 mM), reaching levels of 10–30 mM.[38] To simulate the behavior of FA-SRNPs in a high-GSH environment, the nanoparticles were incubated with 20 mM GSH at 37 °C. TEM revealed nanoparticle disassembly, with irregular particle sizes and partial loss of spherical morphology (Figure 2K). Concurrently, their surface charge changed significantly over time (Figure 2L). These findings indicate that in the high-GSH tumor microenvironment, disulfide bonds in DSPE-SS-PEG on the surface of FA-SRNPs are cleaved, leading to partial detachment of PEG chains and surface restructuring, resulting in changes in surface charge. This process further facilitates the controlled release of R848 at the tumor site, laying a solid foundation for subsequent in vivo studies.

2.2. PDT and PTT Effects

The photothermal performance of FA-SNPs was initially evaluated using infrared thermal imaging. Temperature variations of FA-SNPs solutions at different concentrations were recorded under 1064 nm laser irradiation at a power density of 1.0 W cm^{-2}. The heating curve (**Figure** 3A) and thermal images (Figure 3B) showed that the temperature of the 100 μg mL^{-1} FA-SNPs solution rapidly increased to 62.8 °C after 12 min of irradiation. Even at the lowest concentration (6.25 μg mL^{-1}), the temperature reached 50.1 °C. In contrast, the temperature of the PBS control only increased from 26.8 °C to 31.3 °C under the same conditions. Additionally, 50 μg mL^{-1} FA-SNPs solutions were irradiated with a 1064 nm laser at varying power densities. The heating curve (Figure 3C) and thermal images (Figure 3D) demonstrated that even at a low power of 0.6 W cm^{-2}, the solution temperature increased to 50.7 °C after 10 min and reached 51.1 °C after 12 min of irradiation. At 1.5 W cm^{-2}, the temperature reached a maximum of 65.6 °C after 12 min. In contrast, irradiation of an indocyanine green (ICG) solution (100 μg mL^{-1}) using an 808 nm laser (1.0 W cm^{-2}) resulted in a maximum temperature increase to only 37.4 °C, and the temperature began to decline after 7 min of irradiation (Figure S10, Supporting Information). This result highlights the superior photothermal therapeutic potential of FA-SNPs, which stems from the unique structure of SKCN. Unlike ICG, which lacks a well-defined acceptor-donor framework, SKCN adopts a quinoidal A–D–A structure with a BTP core, significantly enhancing ICT and achieving higher photothermal conversion efficiency. To evaluate the durability of the photothermal effect, a 50 μg mL^{-1} FA-SNPs solution was subjected to five consecutive heating–cooling cycles under 1064 nm laser irradiation at 1.5 W cm^{-2} (Figure 3E). The temperature consistently exceeded 65 °C during each cycle and quickly returned to room temperature upon cessation of the laser. The UV–vis–NIR spectra of FA-SNPs recorded under various heating conditions (Figure 3F) showed minimal changes in the absorption peaks, with no significant shift in the maximum absorption peak. Moreover, the appearance of the FA-SNPs solution remained unchanged after laser irradiation, demonstrating its exceptional stability. In contrast, the ICG solution exhibited noticeable changes in both appearance and UV–vis–NIR after 808 nm laser irradiation (Figure S11, Supporting Information). The stability of organic materials is closely related to their structure. Many infrared molecules rely on alkene bonds to maintain conjugation, which are prone to photoisomerization or photooxidation under illumination.[17b] In contrast, SKCN extends conjugation through a fused-ring structure, not only enhancing molecular rigidity but also significantly improving molecular stability. This structural advantage ensures that SKCN remains stable under prolonged laser irradiation, maintaining its properties and reactivity during phototherapy.[12b] Based on the formula provided in the literature,[39] the photothermal conversion efficiency (η) of FA-SNPs was calculated to be 75.14% (Figure 3G,H), further confirming the outstanding photothermal conversion efficiency of the SKCN-based nanoparticles.

The capacity of FA-SNPs to generate ROS under 1064 nm laser irradiation was systematically assessed. 1,3-Diphenylisobenzofuran (DPBF) was first employed as a probe to detect superoxide anions ($\cdot O_2^-$). DPBF exhibited some photosensitivity, with its absorption peak at 420 nm decreasing to 69% after 25 min of 1.5 W cm^{-2} laser irradiation in the PBS group. As the FA-SNPs concentration increased, the absorption peak further diminished, reaching 34% at 100 μg mL^{-1} (Figure 3I; Figure S12, Supporting Information). The decrease in DPBF absorption was linearly correlated with increased laser power and exposure time, indicating that FA-SNPs generated ROS under 1064 nm irradiation, which effectively degraded DPBF (Figure 3J; Figure S12, Supporting Information). Subsequently, 9,10-anthracenediyl-bis(methylene)dimalonic acid (ABDA) was utilized to evaluate the ability of FA-SNPs to produce singlet oxygen ($^1O_2$) under the same conditions. At a concentration of 100 μg mL^{-1}, the ABDA absorption peak at 400 nm decreased to 51% (Figure 3K; Figure S13, Supporting Information). A similar trend was observed with varying laser powers (Figure 3L; Figure S13, Supporting Information). The ROS generation efficiency of FA-SNPs under 1064 nm laser excitation is higher than that of ICG under 808 nm laser excitation (Figure S14, Supporting Information). According to the energy gap law, as Δ_E decreases, the non-radiative decay rate of the excited state accelerates, intensifying the competition among internal conversion (IC), radiative transition (RT), and intersystem crossing (ISC). Studies have shown that increasing molecular rigidity can stabilize the excited state and balance RT, ISC, and IC.[40] As a fully fused-ring π-conjugated molecule, SKCN exhibits significantly higher rigidity compared to NIR-II phototherapeutic molecules connected by single and double bonds. This enhanced rigidity effectively suppresses vibrational coupling between the S1 and S0 states, allowing excitation energy to transfer more easily to the triplet state via ISC, thereby significantly improving NIR-II PDT performance and demonstrating great potential.[12b]

2.3. In Vitro Antitumor Activity of FA-SNPs and FA-SRNPs

After validating the PTT and PDT therapeutic effects of FA-SNPs, we further investigated their biocompatibility and antitumor potential in vitro. Three different cell lines (ID8, NCM460, and SKOV3) were used to assess the cytotoxicity of FA-SNPs. Cell Counting Kit-8 (CCK-8) assays revealed that, even at a high concentration of 100 μg mL^{-1}, the viability of all three cell lines

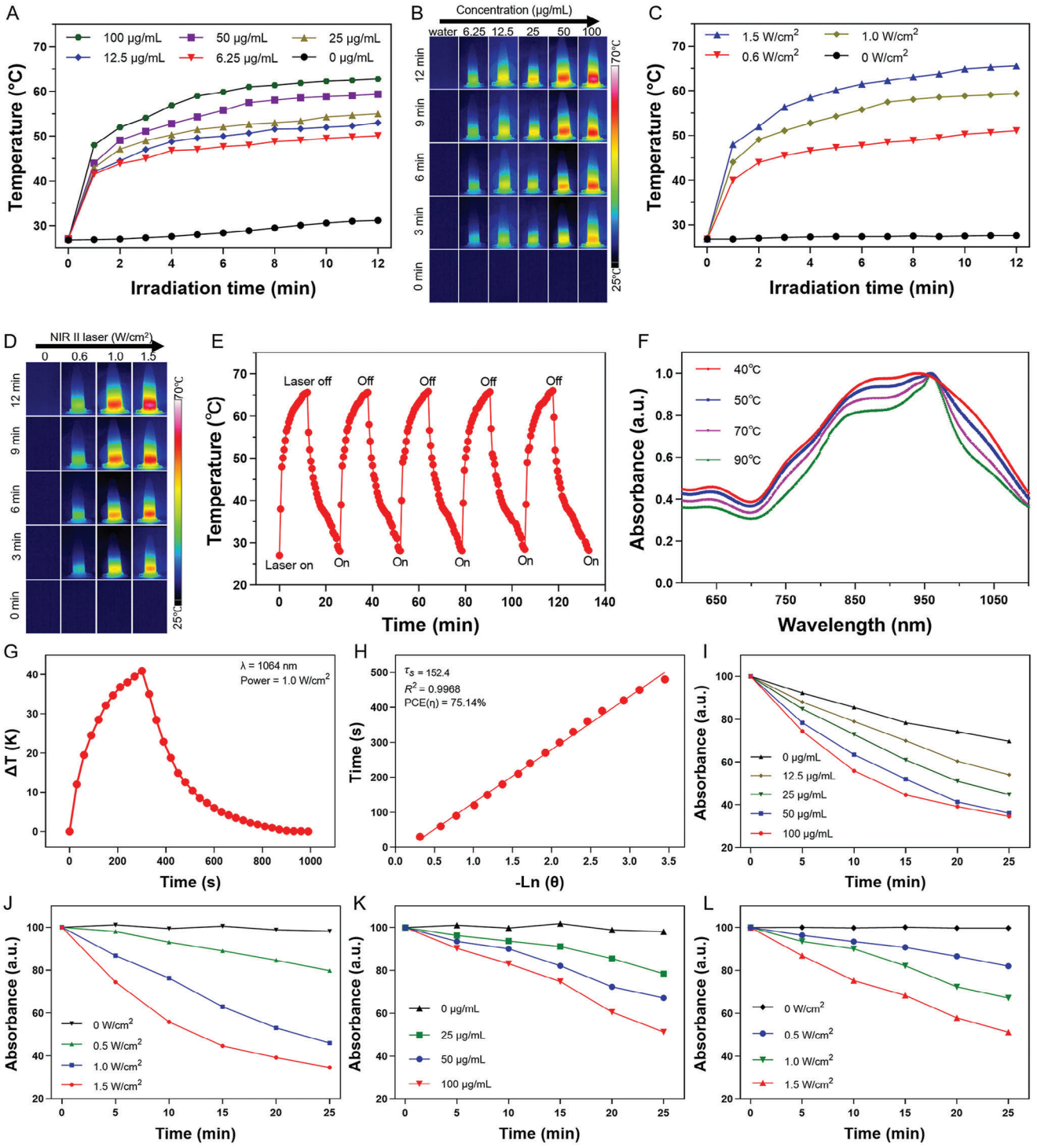

Figure 3. Evaluation of FA-SNPs PTT and PDT effects and photothermal conversion efficiency (η). Temperature changes of FA-SNPs solutions at different concentrations under 1064 nm laser irradiation at 1.0 W cm^{-2} A) and infrared thermal imaging B). temperature changes of FA-SNPs solutions under different laser powers at the same concentration C) and infrared thermal imaging D). E) Five cycles of heating and cooling curves of FA-SNPs solutions with the 1064 nm laser on-off. F) UV–vis absorption spectra of FA-SNPs under different high-temperature conditions. G) Heating and cooling curves of FA-SNPs solutions under 1064 nm laser irradiation. H) Linear relationship between the cooling time and -lnθ with a calculated photothermal conversion efficiency (η) of 75.14%. DPBF absorption peak changes at 420 nm under 1064 nm laser irradiation for different concentrations of FA-SNPs solutions (I) and after irradiation at different powers J). The ABDA absorption peak changes at 400 nm for different concentrations of FA-SNPs solutions under 1064 nm laser irradiation K) and after irradiation at different powers L).

remained above 90% (**Figure** 4A; Figure S15, Supporting Information), indicating good biocompatibility and suitability for biomedical applications. Subsequently, ID8 cells were incubated with varying concentrations of FA-SNPs and exposed to 1064 nm laser irradiation at power densities of 1.0 and 0.6 W cm^{-2} for 5 min per well. The CCK-8 assay results showed a concentration- and power-dependent decrease in cell viability, dropping below 10% at the highest FA-SNPs concentration and laser power. These findings suggest that, while FA-SNPs exhibit low intrinsic cytotoxicity, they can effectively induce cell death upon 1064 nm laser irradiation (Figure 4B). R848, a potent agonist of TLR7/8 receptors, was also assessed for its effect on cell viability. CCK-8 assays showed that R848, even at concentrations up to 200 μg mL^{-1}, did not significantly reduce cell viability (Figure 4C). The cellular uptake of FA-SNPs was then examined to verify the targeting capability of FA conjugation. FA-SNPs demonstrated superior cellular uptake compared to non-FA-conjugated SNPs, with the difference becoming more pronounced over time (Figure 4D; Figure S16, Supporting Information). Quantitative analysis revealed that, after 4 h of incubation, the uptake of FA-SNPs was twice that of SNPs (Figure S17, Supporting Information).

To further confirm the oxidative damage and photodynamic therapeutic effects of SKCN nanoparticles following 1064 nm laser irradiation, 2,7-dichlorofluorescein diacetate (DCFH-DA) was used as a probe to detect intracellular ROS generation. Flow cytometry (FCM) results demonstrated significantly higher ROS production in the FA-SNPs+L and FA-SRNPs+L groups compared to other experimental groups (Figure 4E). Fluorescence microscopy corroborated these findings, revealing intense green fluorescence in both groups, further supported by 3D simulation data (Figure 4F; Figure S18, Supporting Information). PTT-induced heat stress and elevated temperatures can disrupt mitochondrial membrane potential and impair mitochondrial function, while PDT-generated ROS act as critical cytotoxic agents that oxidize and damage DNA double strands. Together, these effects synergistically trigger apoptosis pathways, effectively killing tumor cells.[41] JC-1 staining was used to monitor changes in mitochondrial membrane potential in ID8 cells.[42] Confocal laser scanning microscopy (CLSM) images (Figure 4G) showed that JC-1 existed mainly in monomeric form in the FA-SNPs+L and FA-SRNPs+L groups, resulting in reduced red fluorescence and increased green fluorescence, indicative of mitochondrial depolarization. In contrast, in the PBS, L, and FA-SNPs with R848 groups, JC-1 predominantly existed in its aggregated form, resulting in strong red fluorescence. Quantitative analysis and 3D model data supported these observations (Figures S19 and S20, Supporting Information). γ-H2AX was used as a marker to assess DNA damage in ID8 cells induced by FA-SNPs and FA-SRNPs under 1064 nm laser irradiation. CLSM images (Figure 4H) revealed a substantial amount of green fluorescence on the nuclear surface in the FA-SNPs+L and FA-SRNPs+L groups, whereas no significant green fluorescence was detected in the other groups. Quantitative analysis of green fluorescence intensity further confirmed these results (Figure S21, Supporting Information), demonstrating that FA-SNPs effectively induce DNA damage under laser irradiation.

We employed Calcein/PI staining to evaluate cell viability and cytotoxicity. The results demonstrated that in the FA-SNPs+L and FA-SRNPs+L groups, cells exhibited extensive red fluorescence, indicative of cell death, whereas in the PBS, L, FA-SNPs, and R848 groups, cells predominantly displayed green fluorescence, indicating viable cells (Figure 4I; Figure S22, Supporting Information). To corroborate these results, we conducted Annexin V-FITC apoptosis assays, which revealed significantly elevated early and late apoptosis rates in the FA-SNPs+L and FA-SRNPs+L groups, with late apoptosis rates reaching 68.8% and 70.9%, respectively—substantially higher than those observed in the other groups (Figure 4J). The thermal stress and ROS generated during phototherapy activated P53, which regulated the expression of Bax and Bcl-2, leading to upregulation of Bax and downregulation of Bcl-2, ultimately inducing mitochondria-mediated apoptosis. Western blot analysis showed that in the FA-SNPs+L and FA-SRNPs+L groups, Bax expression increased, while Bcl-2 expression was significantly reduced (Figure 4K; Figure S23, Supporting Information). These findings suggest that SKCN-based nanoparticles, characterized by strong ICT, a narrow bandgap, and high molar extinction coefficient, exhibit potent photothermal and photodynamic therapeutic effects under single 1064 nm laser irradiation. The nanoparticles effectively induce mitochondrial membrane potential disruption and DNA damage, regulating the expression of apoptosis-related proteins, leading to apoptosis, thereby demonstrating their potential as powerful agents for PTT and PDT.

2.4. In Vitro Immune Effects of R848, FA-SNPs, and FA-SRNPs

Phototherapy is widely regarded as one of the primary methods for inducing ICD in tumor cells.[43] During PTT and PDT therapies, dying or near-dead tumor cells release substantial amounts of DAMPs and TAAs, including CRT, which translocates from the endoplasmic reticulum to the cell membrane, and HMGB1, which is released from the nucleus into the extracellular environment. These molecules engage with specific receptors on DCs and macrophages, enhancing antigen presentation and activating specific antitumor immune responses.[44] To assess the effects of phototherapy-induced ICD, we used CLSM to evaluate CRT and HMGB1 fluorescence across different treatment groups. The results revealed significantly higher CRT expression (green fluorescence) in the FA-SNPs+L and FA-SRNPs+L groups compared to the other groups (**Figure** 5A). In contrast, HMGB1 expression on the nuclear surface was markedly reduced in these groups (Figure 5B). Quantitative analyses of green fluorescence for both molecules confirmed these findings (Figures S24 and S25, Supporting Information). These results suggest that SKCN-based nanoparticles, when excited by a 1064 nm laser, enhance oxidative stress through PTT and PDT, effectively inducing ICD in tumor cells.

DCs are key players in tumor immunity, serving as primary antigen-presenting cells (APCs). They recognize, capture, and process tumor antigens, which they subsequently present to T cells, thereby initiating a specific antitumor immune response.[45] R848 is a potent immunomodulator that enhances DC maturation and their antigen-presenting capabilities, promoting the proliferation and activation of T cells, particularly $CD8^+$ cytotoxic T cells.[46] Additionally, R848 effectively induces macrophage polarization toward the M1 phenotype, a critical

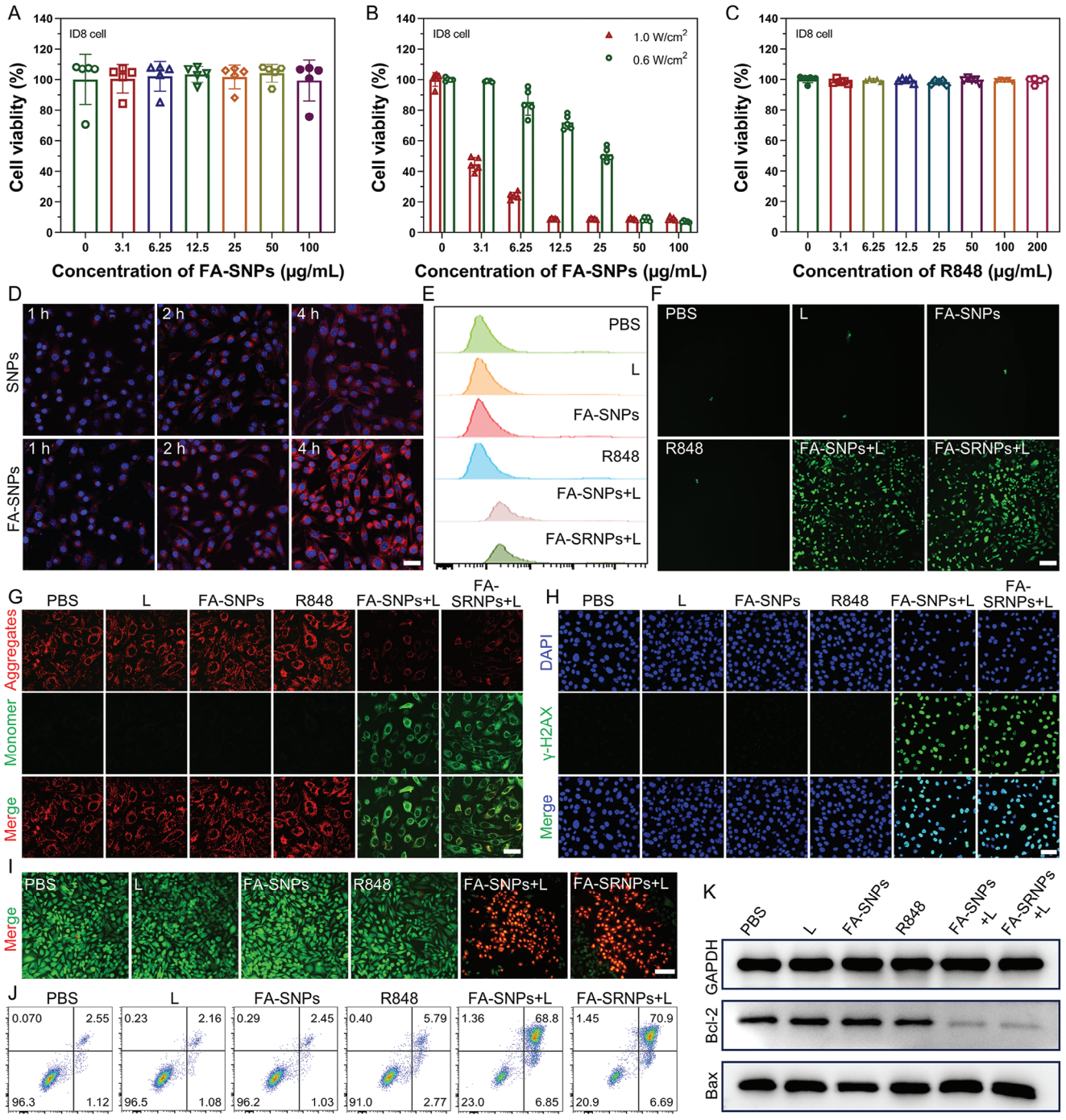

Figure 4. In vivo antitumor effects. A) Effects of different concentrations of FA-SNPs on ID8 cell viability ($n = 5$). B) Effects of different powers of 1064 nm laser irradiation with varying concentrations of FA-SNPs on ID8 cell viability ($n = 5$). C) Effects of different concentrations of R848 on cell viability ($n = 5$). D) CLSM images showing the cellular uptake of m-THPP-labeled SNPs and FA-SNPs in ID8 cells at different time points; scale bar = 50 μm. E) FCM analysis of ROS generation in ID8 cells subjected to different treatments. F) Fluorescence microscopy images showing ROS generation in ID8 cells under different treatments. Scale bar = 200 μm. G) CLSM images showing changes in the mitochondrial membrane potential of ID8 cells stained with JC-1 after different treatments. Scale bar = 50 μm. H) CLSM images showing DNA damage in ID8 cells marked by γ-H2AX under different treatments; scale bar = 50 μm. I) Merged fluorescence microscopy images of live/dead cell staining in different treatment groups; scale bar = 200 μm. J) FCM analysis of apoptosis in ID8 cells subjected to different treatments. K) Western blot images showing the expression of apoptotic proteins Bcl-2 and Bax.

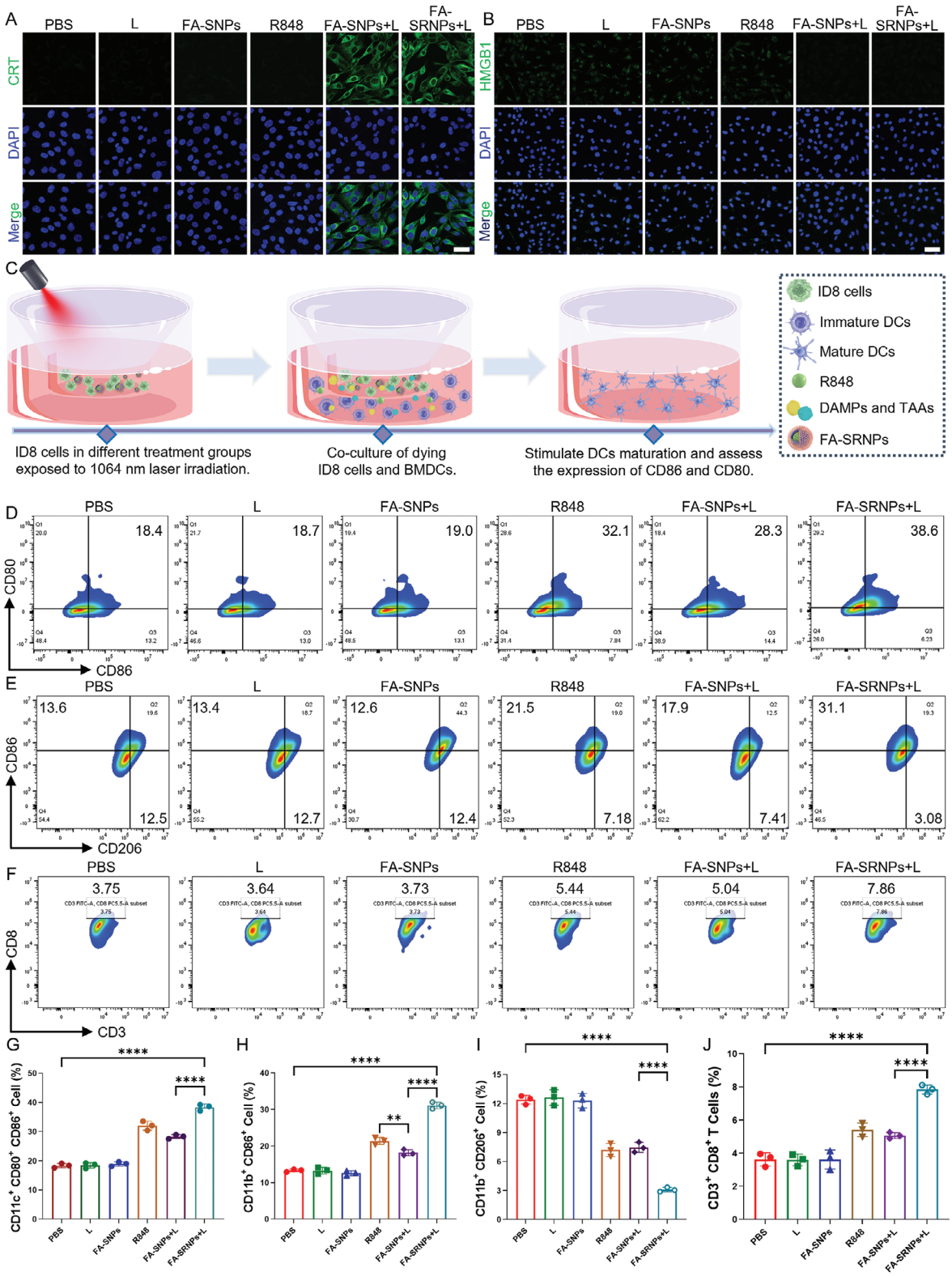

Figure 5. Analysis of induced ICD and the in vitro immune response. Representative CLSM images of CRT exposure (A, scale bar = 50 μm) and HMGB1 expression (B, scale bar = 100 μm) in cells subjected to different treatments. C) Schematic of the Transwell system. FCM analysis of DC maturation D) and quantitative analysis G) in different treatment groups. FCM analysis of macrophages E) with quantitative analysis of M1 (H) and M2 (I) phenotypes and FCM analysis of CTLs F) with quantitative analysis J) across different treatment groups. The data are presented as the means ± SDs. The *p*-values were calculated via one-way analysis of variance (ANOVA), $*p < 0.05$, $**p < 0.01$, $***p < 0.001$, and $****p < 0.0001$.

aspect of tumor immunotherapy.[47] Based on this concept, we combined phototherapy with the immunomodulator R848 to further validate its immunostimulatory effects in vitro. ID8 cells from various treatment groups were cocultured with bone marrow-derived dendritic cells (BMDCs) for 24 h using a transwell system (Figure 5C). FCM analysis revealed that DC maturation ($CD11c^+$ $CD80^+$ $CD86^+$) increased from 18.4% in the PBS group to 32.1% in the R848 group and 28.3% in the FA-SNPs+L group, with the FA-SRNPs+L group showing the highest maturation level at 38.6% (Figure 5D,G; Figure S26, Supporting Information). Macrophage polarization was also assessed, showing that the FA-SRNPs+L group exhibited the strongest ability to polarize M2 macrophages toward the M1 phenotype (Figure 5E,H,I; Figure S27, Supporting Information). Given that $CD8^+$ T lymphocytes are the primary cytotoxic T cells responsible for inducing apoptosis in cancer cells through the secretion of perforin and granzyme, we measured the activation levels of $CD8^+$ T cells ($CD3^+$ $CD8^+$ T cells) in vitro. Compared with the PBS group (3.75%), the R848 group and FA-SNPs+L group showed increased activation levels of 5.44% and 5.04%, respectively, while the FA-SRNPs+L group reached 7.86%, more than doubling the activation observed in the PBS group (Figure 5F,J; Figure S28 Supporting Information). These results indicate that the combination of phototherapy and R848 significantly enhances the antitumor immune response by promoting DC maturation, increasing the expression of costimulatory molecules (CD80/CD86), inducing M1 macrophage polarization, and activating $CD8^+$ cytotoxic T cells.

2.5. Tumor Accumulation, Biodistribution, Photothermal Imaging, Photoacoustic Imaging and Clearance

Targeted accumulation of PTT-PDT agent in malignant tumor tissues can significantly enhance therapeutic efficacy while minimizing damage to surrounding healthy tissues. In earlier experiments, we demonstrated that FA-SNPs exhibit excellent tumor cell uptake capabilities. To further investigate this, we explored the in vivo tumor accumulation and biodistribution of FA-SNPs in a C57BL/6 mouse orthotopic ovarian cancer model. First, fluorescein potassium salt was injected intraperitoneally, and the tumor model's successful establishment was confirmed using an in vivo imaging system (IVIS), clearly identifying the ovarian tumor location (**Figure 6**A, 0 h mouse image). Subsequently, methyl-4-(1-hydroxy-2,2,6,6-tetramethylpiperidin-4-yl)phenyl (m-THPP)-labeled FA-SNPs or SNPs (5 mg kg^{-1}) were administered via tail vein injection, and the fluorescence signal distribution in the mice was monitored over time using the fluorescence imaging system. As shown in Figure 6A, both FA-SNPs and SNPs exhibited gradual accumulation at the tumor site, peaking 8 h post-injection and decreasing by 24 h due to metabolic clearance. However, FA-SNPs demonstrated enhanced tumor targeting compared to SNPs, as confirmed by quantitative analysis of the fluorescence images, which revealed higher tumor accumulation of FA-SNPs (Figure 6B). Dissection of the mice 8 h after injection further confirmed that both types of nanoparticles primarily accumulated at the ovarian tumor site, with FA-SNPs showing superior accumulation compared to SNPs (Figure 6C,D). These results highlight the potential of FA-SNPs for enhanced tumor-specific targeting, improving therapeutic outcomes while reducing off-target effects.

The ovaries of mice are located on both sides of the spine in a relatively fixed position, lying close to the dorsal skin. Measurements show that the combined thickness of the dorsal skin and peritoneum above the ovaries is ≈1 mm (Figure S29, Supporting Information), while the penetration depth of NIR-II light exceeds 1 cm.[48] Therefore, FA-SNPs can be effectively activated by 1064 nm laser irradiation to treat ovarian tumors in mice. To further assess the photothermal imaging and therapeutic efficacy of the nanoparticles under 1064 nm laser irradiation, experiments were conducted with three groups: the L group, FA-SNPs+L group, and FA-SRNPs+L group. After successfully establishing an orthotopic ovarian cancer model in mice, different formulations (5 mg kg^{-1}) were administered via tail vein injection, while the L group received an equivalent volume of PBS. Eight hours post-injection, the tumor tissues were irradiated with a 1064 nm laser at a power density of 0.6 W cm^{-2} for 10 min, ensuring minimal damage to normal tissues. Infrared thermal imaging revealed a significant temperature increase in the tumor regions of the FA-SNPs+L and FA-SRNPs+L groups, reaching 50 °C (Figure 6E; Figure S30, Supporting Information). This result indicates that the method allows for both imaging and the generation of sufficient heat to induce tumor cell death.

Compared to photothermal imaging, NIR-II window photoacoustic imaging offers distinct advantages,[49] including higher spatial resolution, deeper tissue penetration, and reduced tissue scattering.[50] Therefore, we evaluated the photoacoustic imaging performance of FA-SNPs at various concentrations (0, 6.25, 12.5, 25, 50, and 100 μg mL^{-1}) using the MarsSonics PIIP (Photoacoustic Integrated Imaging Platform) in the PA_{1064} channel. The results demonstrated that the photoacoustic signal increased linearly with FA-SNPs concentration (Figure 6F,J). Further validation in the orthotopic ovarian cancer mouse model revealed that after intravenous injection of FA-SNPs (5 mg kg^{-1}), the PA_{1064} signal in the tumor area peaked at 8 h and significantly decreased at 24 h (Figure 6G). These findings suggest that SKCN-based nanoparticles have strong potential as NIR-II photoacoustic probes for detecting deep-seated tumors. This capability is particularly valuable for the diagnosis and treatment of ovarian cancer, a malignancy characterized by hidden, deep abdominal tumors, early detection challenges, and a high propensity for widespread metastasis.

The metabolism and clearance efficiency of nanoparticles are closely related to their size. Nanoparticles with a size of ≈6 nm are typically more readily excreted through the kidneys,[48] whereas larger nanoparticles preferentially accumulate in the liver.[51] To evaluate the metabolic process and long-term biosafety of SNPs, fluorescence imaging was performed on mice after intravenous injection of SNPs via the tail vein. The results showed that SNPs predominantly accumulated in the liver, where they underwent hepatic metabolism. The metabolic products were excreted into the intestines via bile and ultimately eliminated through feces. Fluorescence signals in the liver and feces peaked at 24 h post-administration, gradually weakened over time, and completely disappeared by day 21 (Figure 6H,K,L). Upon dissection on day 21, no fluorescence signals were detected in major organs, ovaries, or the uterus (Figure 6I). Therefore, SNPs are primarily metabolized by the liver and cleared from the body

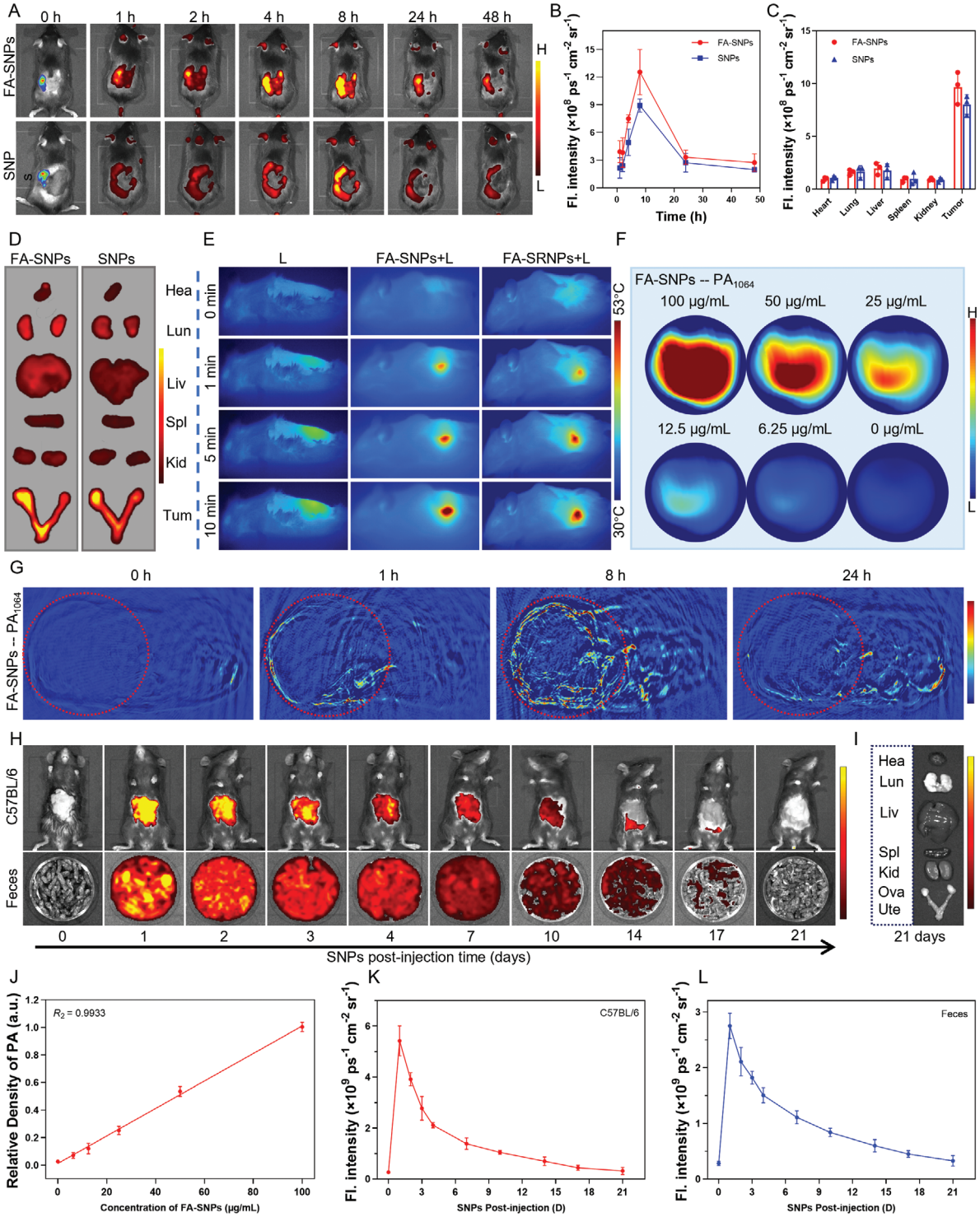

Figure 6. Tumor accumulation, photothermal imaging, photoacoustic imaging, and metabolism. A) Real-time imaging of tumor accumulation and in vivo distribution of m-THPP-labeled FA-SNPs and SNPs in orthotopic ovarian cancer-bearing mice at different time points postinjection. C) Quantitative analysis of fluorescence intensity at the tumor site in the mice ($n = 3$). B) Quantitative analysis of fluorescence intensity in dissected organs ($n = 3$). D) Ex vivo imaging of organs from orthotopic ovarian cancer-bearing mice following intravenous injection of m-THPP-labeled FA-SNPs and SNPs. E) Photothermal imaging of the tumor site in orthotopic ovarian cancer-bearing mice from different treatment groups after intravenous injection. F) Photoacoustic imaging of different concentrations of FA-SNPs in the PA_{1064} channel and J) corresponding quantitative analysis and fitted curve ($n = 3$). G) Time-dependent photoacoustic imaging of the tumor site in orthotopic ovarian cancer-bearing mice following intravenous injection of FA-SNPs in the PA_{1064} channel. H) Fluorescence images of mice and feces at different time points post-injection of SNPs (K,L: corresponding fluorescence quantification, $n = 3$). I) Fluorescence images of major organs from mice on day 21 post-injection of SNPs.

within three weeks, demonstrating excellent long-term biosafety in vivo.

2.6. Evaluation of Antitumor and Antimetastatic Effects In Vivo

In previous experiments, we confirmed that SKCN-based nanoparticles exhibited excellent PTT, PDT, and PIT effects under 1064 nm laser irradiation. Additionally, the immunomodulator R848 significantly promoted the maturation of DCs and M1 macrophage polarization in vitro, further enhancing cytotoxic T lymphocyte activation when combined with phototherapy. Furthermore, the nanoparticles demonstrated strong tumor-targeting capabilities, in vivo photothermal effects, and enhanced photoacoustic signals, highlighting their potential for in vivo cancer treatment. To further assess their therapeutic efficacy against ovarian cancer, we established an orthotopic ovarian cancer mouse model (**Figure 7A**). In subsequent experiments, we prepared R848-loaded nanoparticles, designated as FA-RNPs, using the previously described nanoprecipitation method. This approach aimed to reduce the systemic side effects associated with intravenous R848 administration and to enhance tumor targeting and controlled release in the tumor microenvironment. Following the establishment of the ovarian cancer model, tumor development was monitored using IVIS. The mice were randomly divided into six groups: PBS, PBS+L, FA-SNPs, FA-RNPs, FA-SNPs+L, and FA-SRNPs+L. Treatments were administered intravenously on day 1 (seven days post-cell implantation), with FA-SNPs and FA-SRNPs dosed at 5 mg kg^{-1} and FA-RNPs at 10 mg kg^{-1} in a total volume of 200 µL. Eight hours post-injection, the tumors were irradiated with a 1064 nm laser (0.6 W cm^{-2} for 10 min), and local temperature changes were monitored using a thermal imaging camera. The treatment regimen was repeated on day 3, followed by IVIS to evaluate therapeutic efficacy.

Due to significant metastasis and ascites accumulation observed in some mice from the control group during treatment, the experiment was terminated on day nine. Tumor burden was assessed via IVIS (Figure 7C), followed by dissection of the reproductive organs and measurement of the primary tumor size. In the FA-SNPs+L group, tumors were significantly reduced in four mice, but one mouse experienced tumor recurrence accompanied by metastasis and ascites formation. The FA-SRNPs+L group showed the most significant therapeutic effect, with nearly complete tumor elimination in all five mice and no ascites formation observed (Figure 7B,D). Regular body weight monitoring showed a slight increase in the average weight of mice in the PBS, PBS+L, and FA-SNPs groups, primarily due to substantial ascites accumulation in some mice (Figure 7E). These results indicate that FA-SRNPs combined with PIT demonstrated excellent antitumor efficacy in the orthotopic ovarian cancer model, offering a promising therapeutic strategy for reducing tumor burden and limiting metastasis and ascites formation.

Ascites were collected from the mice, and tumor metastasis in the abdominal cavity and contralateral ovaries was examined. Extensive peritoneal metastases were observed in the PBS, PBS+L, and FA-SNPs groups, consistent with the typical clinical characteristics of ovarian cancer. Metastatic lesions were distributed in the contralateral ovaries, mesentery, inferior edge of the liver and spleen, and uterus. Additionally, some mice accumulated a large volume of ascites, which was either hemorrhagic or pale yellow, with a maximum volume reaching nearly 7 mL. In the FA-RNPs group, although the primary tumor did not significantly shrink, the number of metastatic lesions and the volume of ascites were substantially reduced, attributed to the antitumor immune effects of FA-RNPs (**Figure 8A,B**). Blood analysis revealed decreased red blood cell counts and hemoglobin levels in the PBS, PBS+L, and FA-SNPs groups, likely due to the formation of hemorrhagic ascites(Figure S43, Supporting Information). These groups also exhibited reduced total serum protein levels, indicating mild anemia and hypoproteinemia (Figure S44, Supporting Information). Furthermore, the FA-SRNPs+L group exhibited significantly prolonged survival times, with some mice surviving beyond 100 days, whereas mice in the PBS, L, and FA-SNPs groups had shorter survival times due to rapid ascites accumulation (Figure 8C). These results indicate that FA-SRNPs-based PIT demonstrates excellent long-term efficacy.

Postmortem analysis revealed greater spleen enlargement in the FA-RNPs and FA-SNPs+L groups compared to the PBS group, with the most significant enlargement observed in the FA-SRNPs+L group (Figure 8E). This splenomegaly is likely associated with the release of tumor antigens induced by phototherapy, the generation of ROS, and the immunomodulatory effects of R848, leading to increased lymphocyte aggregation in the spleen. Hematoxylin and eosin (H&E) staining of ovarian tumor tissues showed large areas of tumor necrosis in the FA-SNPs+L and FA-SRNPs+L groups, characterized by marked nuclear condensation, dissolution, and reduced cell density. Terminal deoxynucleotidyl transferase dUTP nick-end labeling (TUNEL) staining further confirmed extensive apoptosis in the necrotic tumor regions, as indicated by the green fluorescence signals (Figure 8D), demonstrating that phototherapy induced significant tumor cell apoptosis. These findings suggest PIT effectively reduces metastasis, limits ascites accumulation, and induces significant tumor cell apoptosis, improving overall therapeutic outcomes in this orthotopic ovarian cancer model.

To further validate the PIT efficacy of FA-SRNPs in other malignancies, an orthotopic breast cancer model was established, given the overexpression of FA in breast cancer.[52] Mice were divided into five groups: PBS, PBS+L, FA-RNPs, FA-SNPs+L, and FA-SRNPs+L. Eight hours after tail vein administration of the formulations, the tumor area was irradiated with a 1064 nm laser (0.6 W cm^{-2} for 10 min). Each group received two treatment sessions (Figure 8F), and body weight and tumor volume were recorded every two days. On day 15, the mice were euthanized, and the tumors were collected and weighed. The results showed progressive tumor growth in the PBS and PBS+L groups, whereas tumor growth was moderately suppressed in the FA-RNPs group. Notably, significant tumor inhibition was observed in the FA-SNPs+L and FA-SRNPs+L groups, with the FA-SRNPs+L group exhibiting the best therapeutic outcomes, as tumors in three mice were nearly eradicated (Figure 8G–I). No significant differences in body weight changes were observed among the groups (Figure S31, Supporting Information). These findings further confirmed the excellent PIT efficacy of FA-SRNPs under 1064 nm laser irradiation.

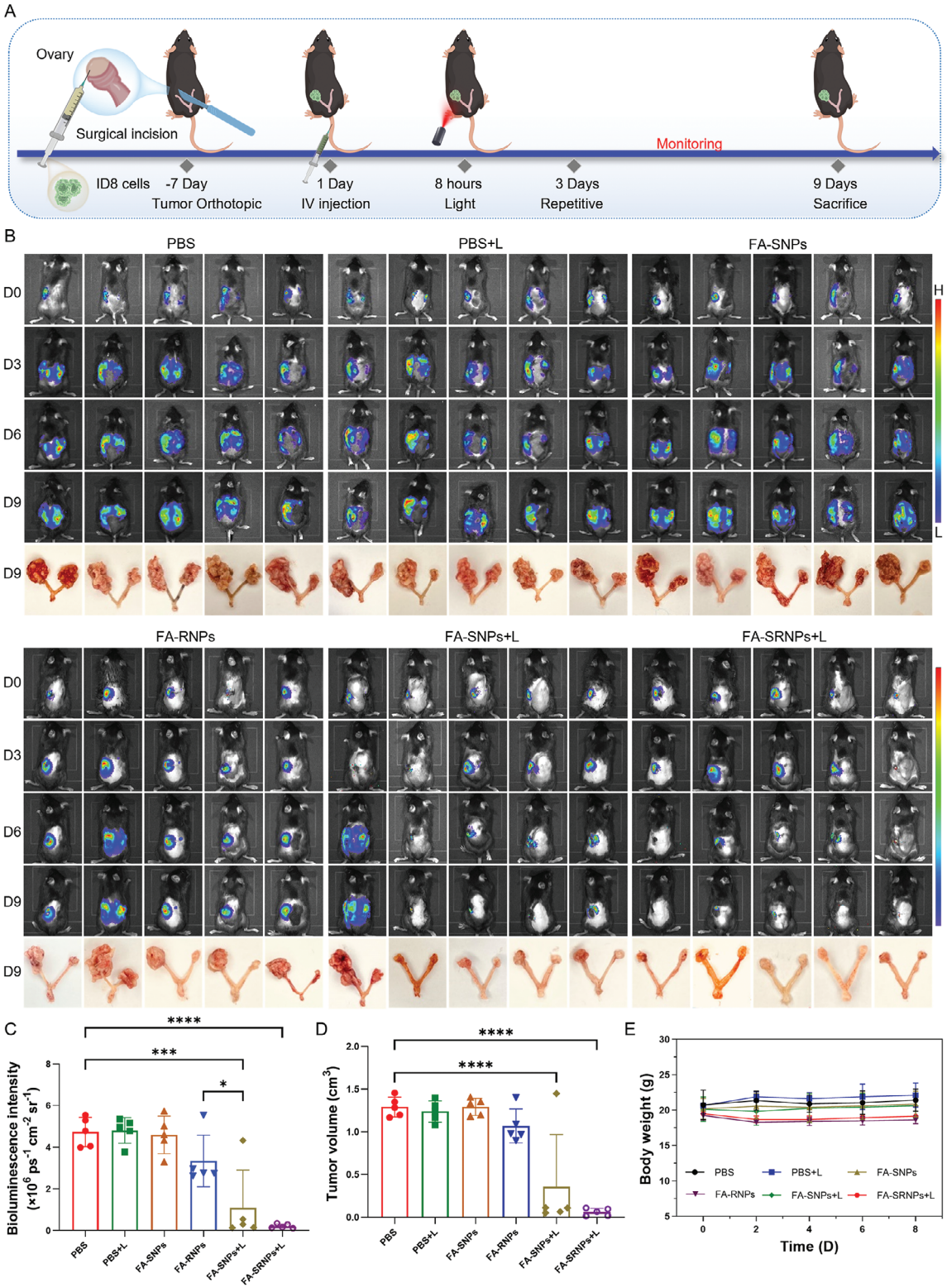

Figure 7. In vivo antitumor effects. A) Schematic representation of the establishment and treatment of the mouse orthotopic tumor model. B) Small animal images of orthotopic ovarian cancer model mice from different treatment groups, with images of reproductive organs dissected at the end of the treatment. C) Quantitative analysis of fluorescence images of the tumor region from small animal images at the end of the treatment ($n = 5$). D) Comparison of primary ovarian tumor diameters at the treatment endpoint ($n = 5$). E) Body weight curves of the mice in the different treatment groups. The data are presented as the means ± SDs. The p values were calculated via one-way analysis of variance (ANOVA), *$p < 0.05$, **$p < 0.01$, ***$p < 0.001$, and ****$p < 0.0001$.

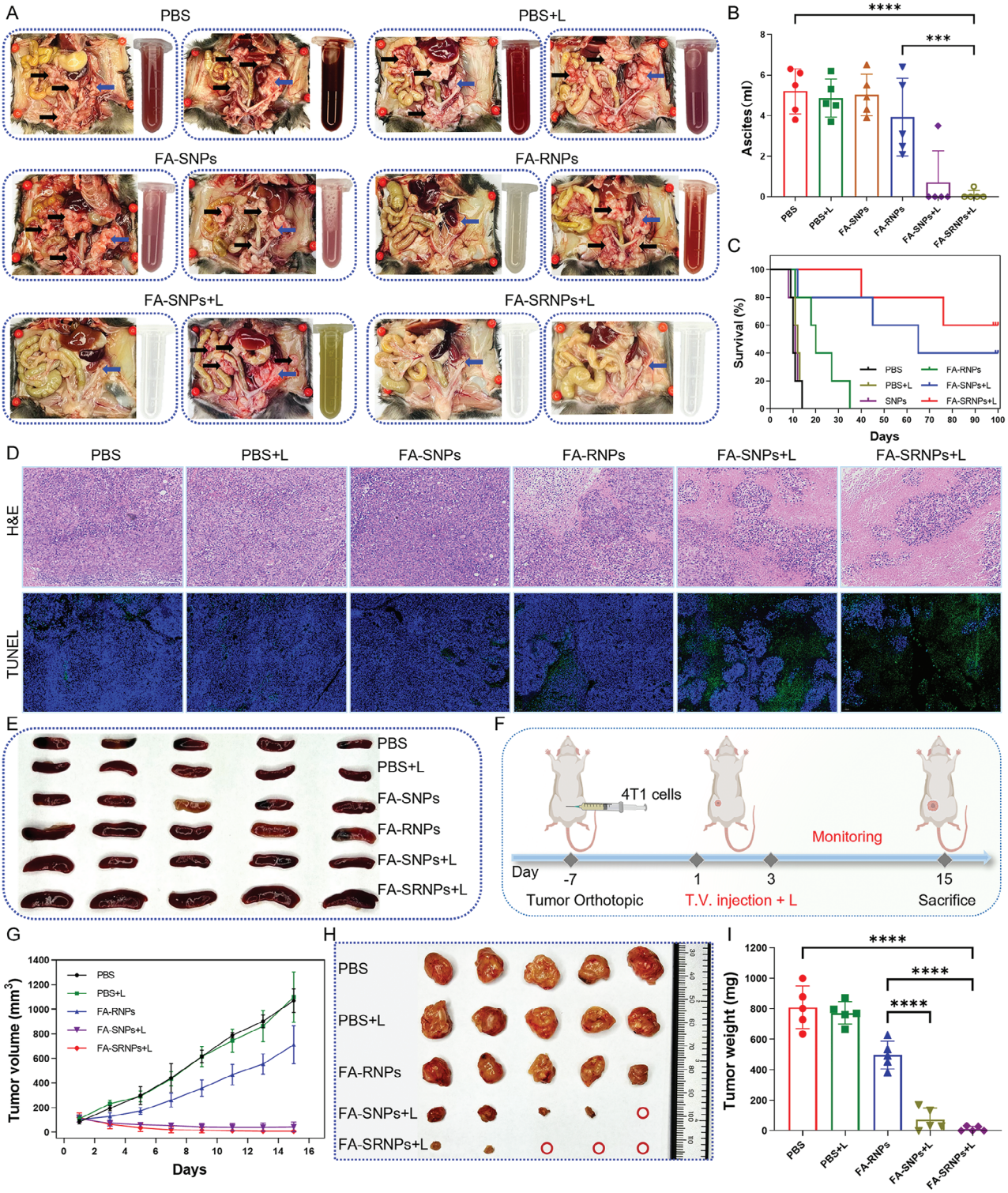

Figure 8. Analysis of in vivo antitumor and antimetastatic effects. A) Comparison of organ metastasis and ascites in the abdominal cavity of mice across different treatment groups (blue arrows indicate primary tumors, black arrows indicate metastatic tumors). B) Comparison of ascites volume between treatment groups. C) Survival curve comparison among the groups. D) Representative H&E and TUNEL staining images of tumors from the different treatment groups. Scale bar = 100 μm. E) Comparison of spleen size in mice across the treatment groups. F) Schematic illustration of the treatment protocol for orthotopic breast cancer-bearing mice. G) Breast tumor growth curves during the treatment period. H) Dissected images of breast tumors at the end of the treatment. I) Tumor weight measurements of breast tumors at the conclusion of the treatment.($n = 5$). The data are presented as the means ± SDs. The p values were calculated via one-way analysis of variance (ANOVA), $^{*}p < 0.05$, $^{**}p < 0.01$, $^{***}p < 0.001$, and $^{****}p < 0.0001$.

2.7. Enhanced Immune Response In Vivo

R848, as a TLR7/8 receptor agonist, regulates the tumor microenvironment by reducing the proportion of immunosuppressive cells such as Tregs and MDSCs.[53] To further explore the in vivo antitumor immune response induced by SKCN-based nanoparticles combined with the immunomodulator R848 under 1064 nm laser irradiation and its impact on the immune microenvironment, we conducted an in-depth analysis of DCs, TAMs, Tregs, M-MDSCs, natural killer cells (NK Cells), $CD4^+$ T cells, and $CD8^+$ T cells within tumors, as well as $CD8^+$ T cells and memory T cells in the spleens of treated mice (**Figure 9A**). First, the proportion of mature DCs in tumors was assessed by FCM. The results revealed a significant increase in the expression of the DC co-stimulatory markers CD80/86 in the FA-RNPs and FA-SNPs+L groups, with the highest proportion observed in the FA-SRNPs+L group at 46.6%, compared to only 15.2% in the PBS group (Figure 9B; Figure S32, Supporting Information). Analysis of TAMs showed a shift from M2-type to M1-type in the FA-RNPs and FA-SNPs+L groups, with the most pronounced changes in the FA-SRNPs+L group. The proportion of M1-type TAMs increased from 10.5% to 30.9%, while M2-type TAMs decreased from 43.5% to 15.9% (Figure 9C; Figures S33 and S34, Supporting Information). The maturation of DCs and polarization of M1 macrophages effectively activated cytotoxic T lymphocytes in tumors. Consequently, the proportion of $CD45^+$ $CD3^+$ $CD8^+$ T cells was evaluated. The FA-RNPs and FA-SNPs+L groups exhibited $CD8^+$ T cell proportions of 16.2% and 14.3%, respectively, while the FA-SRNPs+L group showed a significantly higher proportion of 21.9%, compared to only 7.97% in the PBS group (Figure 9D; Figure S35, Supporting Information). Additionally, the proportion of NK cells in the tumor microenvironment increased, with the FA-SRNPs+L group showing 7.66% compared to 4.32% in the PBS group (Figure 9E; Figure S36, Supporting Information).

To further verify the regulation of immunosuppressive cells in the tumor microenvironment, the proportion of M-MDSCs in the FA-RNPs and FA-SNPs+L groups was reduced to 14% and 12.5%, respectively, compared to 20.2% in the PBS group, while the FA-SRNPs+L group exhibited the lowest proportion at 8.24% (Figure 9F; Figure S37, Supporting Information). Similarly, the proportion of Tregs significantly decreased to 7.89% in the FA-SRNPs+L group, compared to 32.7% in the PBS group (Figure 9G; Figure S38, Supporting Information). Moreover, the proportion of $CD4^+$ T cells in the FA-SRNPs+L group increased by more than twofold compared to the PBS group (Figures S38 and S39, Supporting Information). In the spleens, the proportions of $CD8^+$ T cells were 33.5% in the FA-RNPs group and 31.7% in the FA-SNPs+L group, with the highest proportion of 38.5% observed in the FA-SRNPs+L group, markedly higher than the 21.1% seen in the PBS group (Figure 9H; Figure S40, Supporting Information). Further analysis of effector memory T cells (T_{em}, $CD44^+$ $CD62L^-$) and central memory T cells (T_{cm}, $CD44^+$ $CD62L^+$) in the spleens revealed that the FA-SRNPs+L group exhibited a significant increase in Tem cells, from 8.95% in the PBS group to 28.1%, while the proportion of Tcm cells increased from 8.23% to 16% (Figure 9I; Figures S41 and S42, Supporting Information).

In conclusion, SKCN and R848-based nanoparticles, under 1064 nm laser irradiation, significantly enhanced the anti-tumor immune response against ovarian cancer. This therapy stimulated the maturation of DCs and polarization of M1-type TAMs, promoted the activation of $CD8^+$ and $CD4^+$ T cells as well as NK cells, while reducing the proportion of Tregs and M-MDSCs in the tumor microenvironment. Additionally, this therapy elevated the levels of cytotoxic T lymphocytes and memory T cells in the spleen. The combined therapy not only enhanced the immediate immune response but also established a durable immune memory, significantly reducing the occurrence of peritoneal metastasis. These results suggest that this treatment strategy holds promise for the effective management of ovarian cancer and prevention of its widespread metastasis.

2.8. In Vivo Biosafety Analysis

In this study, we conducted a comprehensive in vivo biosafety assessment of SKCN-based nanoparticles, focusing on their effects on hematological parameters and the histology of major organs. In addition to the previously mentioned anemia and hypoproteinemia, a slight increase in white blood cell count was observed in the FA-SRNPs+L group, which may be linked to an inflammatory response induced by phototherapy and R848. However, platelet counts, as well as liver and kidney function indicators, remained within normal ranges, suggesting that the material did not induce significant systemic toxicity (Figures S43 and S44, Supporting Information). Hematoxylin and eosin (H&E) staining was also performed on major organs, including the heart, liver, kidneys, lungs, and spleen, to assess potential morphological changes. Microscopic examination revealed no significant pathological alterations in these tissue sections, with intact cellular structures and no evidence of inflammatory infiltration or cell necrosis (Figure S45, Supporting Information). Collectively, these findings indicate that SKCN-based nanoparticles exhibit excellent in vivo biosafety under the experimental conditions, providing a strong basis for their further clinical application, particularly in the treatment of malignant tumors such as ovarian cancer.

3. Conclusion

In summary, this study is the first to construct the SKCN molecule with a quinoidal A-D-A structure. First, as an A-D-A type molecule, SKCN employs the D-A alternating strategy, which promotes ICT. This strategy effectively reduces the energy gap and leads to red-shifted absorption, a widely adopted approach for designing red-shifted molecules. The enhanced ICT in SKCN ensures strong absorption in the NIR-II region, making it highly suitable for phototherapy applications. Second, beyond the conventional D-A strategy, SKCN incorporates a quinone-based design. The quinone structure minimizes bond length alternation within the molecule, allowing π-electrons to escape the constraints of aromaticity and become more delocalized. This delocalization further reduces the bandgap, resulting in a significant red shift. In SKCN, the large conjugated backbone forms a pronounced quinoidal structure, amplifying its quinoidal properties. Remarkably, even with malononitrile as the acceptor (A) unit, SKCN exhibits a red shift of nearly 200 nm compared to

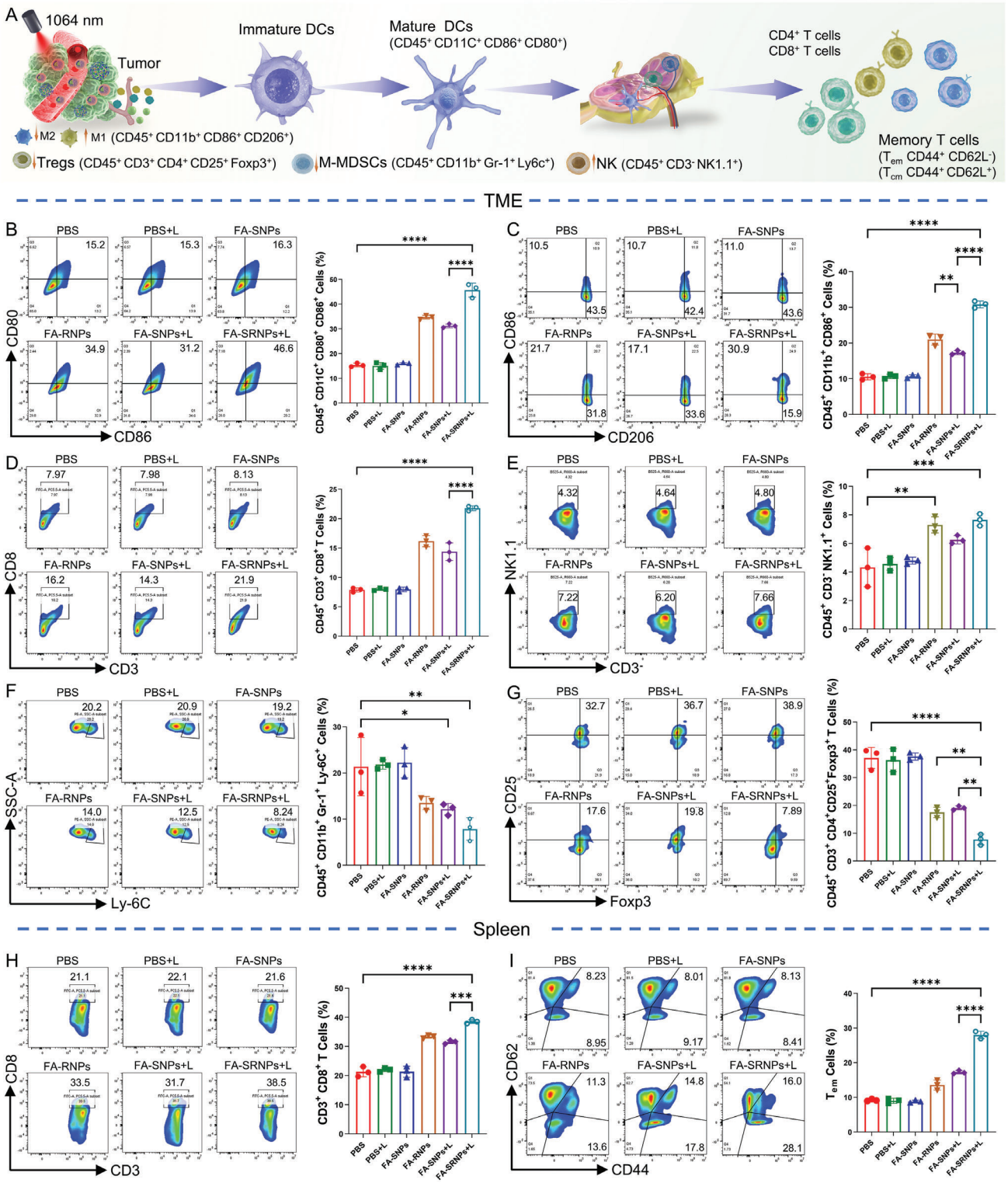

Figure 9. In vivo immune response. A) Regulation of immune cells by photoimmunotherapy. B) FCM analysis of intratumoral DC maturation and quantitative analysis. C) FCM analysis of intratumoral macrophage differentiation and quantitative analysis of M1-type macrophages. D) FCM analysis of intratumoral $CD8^+$ T cells and quantitative analysis. E) FCM analysis of intratumoral NK cells and quantitative analysis. F) FCM analysis of intratumoral M-MDSCs and quantitative analysis. G) FCM analysis of intratumoral Tregs and quantitative analysis. H) FCM analysis of splenic $CD8^+$ T cells and quantitative analysis. I) FCM analysis of splenic memory T cells and quantitative analysis of T_{cm} ($n = 3$). The data are presented as the means ± SDs. The p values were calculated via one-way ANOVA, $^*p < 0.05$, $^{**}p < 0.01$, $^{***}p < 0.001$, and $^{****}p < 0.0001$.

the weak quinone-like Y6 configuration. This highlights the effectiveness of the quinone-based strategy in achieving strong NIR-II absorption. Third, according to the energy gap law, as the energy gap (ΔE) decreases, non-radiative decay rates increase, making internal conversion (IC) more competitive with radiative transition (RT) and intersystem crossing (ISC). To address this, SKCN's all-fused-ring π-conjugated structure provides a completely fixed conformation, significantly enhancing molecular rigidity. Compared to most NIR-II phototherapeutic molecules connected by single or double bonds, SKCN's rigidity suppresses strong vibrational coupling between the S1 and S0 states caused by molecular conformational changes. This stabilization of the excited state ensures that the excited energy is more efficiently channeled into ISC, facilitating energy transfer to the triplet excited state (T1). Consequently, SKCN achieves a better balance between RT, ISC, and IC, enhancing its performance in NIR-II photodynamic therapy by promoting ROS generation. Forth, many infrared molecules rely on alkene bonds to maintain conjugation, but these bonds are prone to photoisomerization or photooxidation under illumination. In basic conditions, vinyl linkers may break, and adjacent-H may be attacked, compromising molecular stability. In contrast, SKCN extends conjugation through fused rings, which not only enhances rigidity but also significantly improves molecular stability. This structural advantage ensures that SKCN remains stable under prolonged laser irradiation, maintaining its properties and reactivity during phototherapy.

Calculations show that SKCN's $O_{H/L}$ value is higher than that of Y6, with a high molar extinction coefficient and a photothermal conversion efficiency (η) of 75.14%. Based on these excellent properties, SKCN was formulated into high-performance nanoparticles, FA-SNPs and FA-SRNPs, which demonstrated outstanding tumor-targeting ability and NIR-II photoacoustic imaging performance, making them suitable for the early diagnosis of deep-seated tumors such as ovarian cancer. Under 1064 nm laser irradiation, these nanoparticles exhibited excellent PTT and PDT effects. Combined with the immunomodulator R848, they significantly promoted the maturation and antigen presentation of DCs, effectively induced M1 macrophage polarization, and activated $CD8^+$ cytotoxic T cells. In an in vivo orthotopic ovarian cancer mouse model, the FA-SRNPs+L group further regulated the tumor immune microenvironment, reduced the infiltration of Tregs and M-MDSCs, enhanced the antitumor activity of $CD4^+$ and $CD8^+$ T cells as well as NK cells, and significantly inhibited peritoneal metastasis and ascites formation. Furthermore, it also demonstrated good therapeutic efficacy in an orthotopic breast cancer model. This study provides strong evidence for the potential application of quinoidal A-D-A molecules in cancer PIT.

4. Experimental Section

Synthesis of FA-SNPs, FA-RNPs, and FA-SRNPs: In this study, three different types of nanoparticles, FA-SNPs, FA-RNPs, and FA-SRNPs, were synthesized via the nanoprecipitation method. Briefly, 20 mg of DSPE-mPEG, 10 mg of DSPE-SS-PEG, and 10 mg of DSPE-PEG-FA were codissolved in 0.9 ml of THF. Concurrently, 0.5 mg of SKCN was dissolved in 0.3 ml of THF. After both solutions were sonicated in a water bath for 5 min, they were mixed and immediately added to a 10 ml aqueous THF solution (THF to water ratio of 1:9) and sonicated for another 15 min. The mixture was then placed in an orbital shaker overnight to evaporate the THF. The solution was filtered through a 0.45 µm pore size filter and subsequently centrifuged three times in a Millipore ultrafiltration tube with ultrapure water. The upper layer of the filtrate, containing FA-SNPs, was collected. The concentrations of the samples were recalculated on the basis of their UV absorption peaks against a standard curve. FA-SRNPs were obtained with a mass ratio of R848 to SKCN of 1 mg:0.5 mg, and FA-RNPs were obtained with 1 mg of R848.

In Vitro Cytotoxicity Assays: This study evaluated the cytotoxicity of FA-SNPs in ID8, NCM460, and SKOV3 cells. The cells were seeded at a density of 1×10^4 cells per well in a 96-well plate and cultured for 12 h. The medium was subsequently replaced with 100 µl of fresh medium containing various concentrations of FA-SNPs (0, 3.1, 6.25, 12.5, 25, 50, or 100 µg mL^{-1}), and the mixture was incubated for 24 h before the addition of CCK-8 and incubation for an additional 2 h. The biocompatibility of FA-SNPs was assessed by measuring the absorbance peak of CCK-8 at 450 nm. The same protocol was used to conduct cytotoxicity tests with R848 in ID8 cells at concentrations of 0, 3.1, 6.25, 12.5, 25, 50, 100, and 200 µg mL^{-1}. Additionally, the effects of FA-SNPs combined with 1064 nm laser irradiation on cell viability were assessed. After coincubating the ID8 cells with various concentrations of FA-SNPs for 12 h, they were exposed to different power settings of the 1064 nm laser (0.6, 1.0 W cm^{-2}) for 5 min per well. Following an additional 12 h of incubation, cell viability was evaluated via the CCK-8 assay.

Establishment of an Orthotopic Ovarian Cancer Model in Mice: This study utilized female C57BL/6 mice, aged 6–8 weeks, procured from SPF (Beijing) Biotechnology Co., Ltd. The mice were maintained in a specific pathogen-free environment with the temperature regulated at 23–26 °C and the humidity maintained between 40–60% under a 12 h light/12 h dark cycle. Each cage housed 3–5 mice, which were allowed free access to food and water. Upon the conclusion of the experiments, the mice were euthanized by cervical dislocation following anesthesia. All animal procedures adhered to the guidelines for the use and care of laboratory animals at Tianjin University and were approved by the Tianjin University Institutional Animal Care and Use Committee (IACUC), with the approval number TJUE-2024-308.

In this investigation, an orthotopic ovarian cancer model was developed in C57BL/6 mice to more accurately replicate the clinical characteristics of ovarian cancer. The procedure began with the removal of the dorsal fur followed by anesthesia with isoflurane. The mice were positioned prone, and the lower back area near the left side of the spine at the level of the hind limb root was disinfected with alcohol. An incision through the skin and peritoneum exposed the ovary, into which 10 µL of a PBS solution containing 5×10^6 ID8-LUC cells was injected. The ovary was then repositioned into the abdominal cavity, and the incision was sutured. This established a syngeneic orthotopic tumor model. The progression of the tumor and the effectiveness of subsequent treatments were monitored via an IVIS, which tracked the bioluminescence of the tumors.

Antitumor Therapy Efficacy: Following the successful establishment of an orthotopic ovarian cancer model in mice via the described methods, tumor growth was monitored via an IVIS. The mice were anesthetized with isoflurane and intraperitoneally injected with 100 µL of 10 mg mL^{-1} D-luciferin for bioluminescence detection. Treatment on the basis of bioluminescence imaging began on day 7 postcell implantation (the first day of treatment), and the mice were divided into six groups: the PBS, PBS+L, FA-SNPs, FA-RNPs, FA-SNPs+L, and FA-SRNPs+L groups. The FA-RNPs group was included to mitigate the systemic side effects of R848, as R848 was formulated into nanoparticles via the nanoprecipitation method. All treatment groups received intravenous injections through the tail vein, with doses of 5 mg kg^{-1} for FA-SNPs and FA-SRNPs and 10 mg kg^{-1} for FA-RNPs, for a total volume of 200 µL. Eight hours postinjection, the laser groups received 1064 nm laser irradiation at the ovarian tumor sites identified via bioluminescence at a power of 0.6 W cm^{-2} for 10 min. Thermal imaging was used to monitor and record the temperature changes in the tumor areas. The same treatment was repeated on day 3. Treatment efficacy and ascites development were assessed through in vivo imaging and observation of abdominal distension, with mouse body weight recorded every two days. On day 9, the mice were euthanized, and the abdominal and reproductive organs were dissected to measure the ovarian tumor size

and calculate the tumor volume. Ascites was collected, and abdominal metastasis was examined. Tumor tissues were analyzed via H&E staining and TUNEL staining. Additionally, another batch of mice was subjected to the same protocol, and survival rates were monitored to generate survival curves.

Supporting Information

Supporting Information is available from the Wiley Online Library or from the author.

Acknowledgements

G.N., G.S., and Y.K. contributed equally to this work. This study was financially supported by a grant from the National Natural Science Foundation of China (Grant No. 32071322), National Natural Science Funds for Excellent Young Scholars (Grant No. 32122044), Technology & Innovation Commission of Shenzhen Municipality (Grant No. JCYJ20210324113004010), and Henan Polytechnic University Youth Innovation Exploratory Fund (Grant NO. NSFRF230414).

Conflict of Interest

The authors declare no conflict of interest.

Data Availability Statement

The data that support the findings of this study are available from the corresponding author upon reasonable request.

Keywords

NIR-II excitation, orthotopic and metastatic ovarian Cancer, photoacoustic imaging, photoimmunotherapy, quinoidal acceptor-donor-acceptor molecule

Received: October 6, 2024
Revised: November 26, 2024
Published online:

[1] a) F. Bray, M. Laversanne, H. Sung, J. Ferlay, R. L. Siegel, I. Soerjomataram, A. Jemal, *CA Cancer J. Clin.* **2024**, *74*, 229; b) P. M. Webb, S. J. Jordan, *Nat. Rev. Clin. Oncol.* **2024**, *21*, 389.

[2] Z. R. C. Marks, N. K. Campbell, N. E. Mangan, C. J. Vandenberg, L. J. Gearing, A. Y. Matthews, J. A. Gould, M. D. Tate, G. Wray-McCann, L. Ying, S. Rosli, N. Brockwell, B. S. Parker, S. S. Lim, M. Bilandzic, E. L. Christie, A. N. Stephens, E. de Geus, M. J. Wakefield, G.-Y. Ho, O. McNally, D. Bowtell, P. Webb, A. DeFazio, N. Traficante, S. Fereday, L. Bowes, J. Hendley, I. A. McNeish, D. D. L. Bowtell, et al., *Nature* **2023**, *620*, 1063.

[3] L. Wang, X. Wang, X. Zhu, L. Zhong, Q. Jiang, Y. Wang, Q. Tang, Q. Li, C. Zhang, H. Wang, D. Zou, *Mol. Cancer* **2024**, *23*, 66.

[4] A. C. Veneziani, E. Gonzalez-Ochoa, H. Alqaisi, A. Madariaga, G. Bhat, M. Rouzbahman, S. Sneha, A. M. Oza, *Nat. Rev. Clin. Oncol.* **2023**, *20*, 820.

[5] a) Z. Zhang, Y. Du, X. Shi, K. Wang, Q. Qu, Q. Liang, X. Ma, K. He, C. Chi, J. Tang, B. Liu, J. Ji, J. Wang, J. Dong, Z. Hu, J. Tian, *Nat. Rev. Clin. Oncol.* **2024**, *21*, 449; b) J. Ma, N. Li, J. Wang, Z. Liu, Y. Han, Y. Zeng, *Exploration* **2023**, *3*, 20220161.

[6] a) P. Mroz, A. Yaroslavsky, G. B. Kharkwal, M. R. Hamblin, *Cancers (Basel)* **2011**, *3*, 2516; b) H. Li, Y. Kim, H. Jung, J. Y. Hyun, I. Shin, *Chem. Soc. Rev.* **2022**, *51*, 8957.

[7] L. Lv, B. Fan, X. Ji, Y. Liu, T. Chen, Y. Li, X. Gao, P. Chen, B. Tang, G. Chen, *Coordin. Chem. Rev.* **2024**, *507*, 215733.

[8] a) J. Yuan, Y. Zhang, L. Zhou, G. Zhang, H. L. Yip, T.-K. Lau, X. Lu, C. Zhu, H. Peng, P. A. Johnson, M. Leclerc, Y. Cao, J. Ulański, Y. Li, Y.-P. Zou, *Joule* **2019**, *3*, 1140; b) G. Zhang, J. Zhao, P. C. Y. Chow, K. Jiang, J. Zhang, Z. Zhu, J. Zhang, F. Huang, H. Yan, *Chem. Rev.* **2018**, *118*, 3447.

[9] L. Zhu, J. Zhang, Y. Guo, C. Yang, Y. Yi, Z. Wei, *Angew. Chem., Int. Ed. Engl.* **2021**, *60*, 15348.

[10] Z. Y. Yao, X. J. Wan, C. X. Li, Y. S. Chen, *Accounts Mater. Res.* **2023**, *4*, 772.

[11] a) Y. Jiang, S. Sun, R. Xu, F. Liu, X. Miao, G. Ran, K. Liu, Y. Yi, W. Zhang, X. Zhu, *Nat. Energy* **2024**, *9*, 975; b) Z. Zheng, J. Wang, P. Bi, J. Ren, Y. Wang, Y. Yang, X. Liu, S. Zhang, J. Hou, *Joule* **2022**, *6*, 171; c) L. Zhu, M. Zhang, G. Zhou, Z. Wang, W. Zhong, J. Zhuang, Z. Zhou, X. Gao, L. Kan, B. Hao, F. Han, R. Zeng, X. Xue, S. Xu, H. Jing, B. Xiao, H. Zhu, Y. Zhang, F. Liu, *Joule* **2024**, *8*, 3153; d) Y. Sun, L. Wang, C. Guo, J. Xiao, C. Liu, C. Chen, W. Xia, Z. Gan, J. Cheng, J. Zhou, Z. Chen, J. Zhou, D. Liu, T. Wang, W. Li, *J. Am. Chem. Soc.* **2024**, *146*, 12011.

[12] a) G. Song, W. Feng, Y. Li, H. Liang, Z. Li, B. Kan, X. Wan, Z. Yao, C. Li, Y. Chen, *Chem. Commun.* **2023**, *59*, 10307; b) Y. Zhang, Y. Yu, X. Liu, J. Miao, Y. Han, J. Liu, L. Wang, *Adv. Mater.* **2023**, *35*, 2211714.

[13] a) B. Fan, F. Lin, X. Wu, Z. Zhu, A. K. Y. Jen, *Acc. Chem. Res.* **2021**, *54*, 3906; b) F. Lin, K. Jiang, W. Kaminsky, Z. Zhu, A. K. Y. Jen, *J. Am. Chem. Soc.* **2020**, *142*, 15246.

[14] B. Yin, X. Zhou, Y. Li, G. Hu, W. Wei, M. Yang, S. Jeong, W. Deng, B. Wu, Y. Cao, B. Huang, L. Pan, X. Yang, Z. Fu, Y. Fang, L. Shen, C. Yang, H. Wu, L. Lan, F. Huang, Y. Cao, C. Duan, *Adv. Mater.* **2024**, *36*, 2310811.

[15] H. S. Jung, P. Verwilst, A. Sharma, J. Shin, J. L. Sessler, J. S. Kim, *Chem. Soc. Rev.* **2018**, *47*, 2280.

[16] Y. L. Sun, Y. L. Guo, Y. Q. Liu, *Mat. Sci. Eng. R* **2019**, *136*, 13.

[17] a) M. Yang, B. Yin, G. Hu, Y. Cao, S. Lu, Y. Chen, Y. He, X. Yang, B. Huang, J. Li, B. Wu, S. Pang, L. Shen, Y. Liang, H. Wu, L. Lan, G. Yu, F. Huang, Y. Cao, C. Duan, *Chem* **2024**, *10*, 1425; b) X. Zhu, S. Liu, Q. Yue, W. Liu, S. Sun, S. Xu, *CCS Chemistry* **2021**, *3*, 1070.

[18] X. Zhou, C. Shi, S. Long, Q. Yao, H. Ma, K. Chen, J. Du, W. Sun, J. Fan, B. Liu, L. Wang, X. Chen, L. Sui, K. Yuan, X. Peng, *ACS Cent. Sci.* **2023**, *9*, 1679.

[19] X. S. Li, J. F. Lovell, J. Yoon, X. Y. Chen, *Nat. Rev. Clin. Oncol.* **2020**, *17*, 657.

[20] a) X. Zhang, B. Yang, Q. Ni, X. Chen, *Chem. Soc. Rev.* **2023**, *52*, 2886; b) G. Niu, H. Wang, Y. Zhai, B. Zhou, Y. Kang, Z. Pei, X. Ji, *Nano Today* **2024**, *56*, 102286.

[21] a) L. Liu, Y. Pan, L. Ye, C. Liang, X. Mou, X. Dong, Y. Cai, *Coordin. Chem. Rev.* **2024**, *517*, 216006; b) L. Galluzzi, E. Guilbaud, D. Schmidt, G. Kroemer, F. M. Marincola, *Nat. Rev. Drug Discovery* **2024**, *23*, 445.

[22] X. Ren, H. Yao, J. Sun, F. Xue, L. Cui, Y. Xu, K. Sakurai, N. Shen, Z. Tang, *Nano Today* **2024**, *57*, 102402.

[23] a) X. Zhang, Z. Wei, T. Yong, S. Li, N. Bie, J. Li, X. Li, H. Liu, H. Xu, Y. Yan, B. Zhang, X. Chen, X. Yang, L. Gan, *Nat. Commun.* **2023**, *14*, 5653; b) J. Sun, Z. Liu, H. Yao, H. Zhang, M. Zheng, N. Shen, J. Cheng, Z. Tang, X. Chen, *Adv. Mater.* **2023**, *35*, 2207733.

[24] S. H. Bhagchandani, F. Vohidov, L. E. Milling, E. Y. Tong, C. M. Brown, M. L. Ramseier, B. Liu, T. B. Fessenden, H. V. Nguyen, G. R. Kiel, L. Won, R. S. Langer, S. Spranger, A. K. Shalek, D. J. Irvine, J. A. Johnson, *Sci. Adv.* **2023**, *9*, adg2239.

[25] K. N. Moore, A. Angelergues, G. E. Konecny, Y. García, S. Banerjee, D. Lorusso, J. Y. Lee, J. W. Moroney, N. Colombo, A. Roszak, J. Tromp, T. Myers, J. W. Lee, M. Beiner, C. M. Cosgrove, D. Cibula, L. P. Martin, R. Sabatier, J. Buscema, P. Estévez-García, L. Coffman, S. Nicum, L.

R. Duska, S. Pignata, F. Gálvez, Y. Wang, M. Method, A. Berkenblit, D. Bello Roufai, T. Van Gorp, *N. Engl. J. Med.* **2023**, *389*, 2162.
[26] a) G. M. van Dam, G. Themelis, L. M. Crane, N. J. Harlaar, R. G. Pleijhuis, W. Kelder, A. Sarantopoulos, J. S. de Jong, H. J. Arts, A. G. van der Zee, J. Bart, P. S. Low, V. Ntziachristos, *Nat. Med.* **2011**, *17*, 1315; b) J. L. Tanyi, L. M. Randall, S. K. Chambers, K. A. Butler, I. S. Winer, C. L. Langstraat, E. S. Han, A. L. Vahrmeijer, H. S. Chon, M. A. Morgan, M. A. Powell, J. H. Tseng, A. S. Lopez, R. M. Wenham, *J. Clin. Oncol.* **2023**, *41*, 276.
[27] Q. Wang, J. Guan, J. Wan, Z. Li, *RSC Adv.* **2020**, *10*, 24397.
[28] S. Zeng, Z. H. Guo, Y. F. Hao, Y. S. Kafuti, Z. Yang, Q. C. Yao, J. Y. Wang, X. J. Peng, H. D. Li, *Coordin. Chem. Rev.* **2024**, *509*, 215786.
[29] a) S. Zhang, H. Chen, L. Wang, X. Qin, B. P. Jiang, S. C. Ji, X. C. Shen, H. Liang, *Angew. Chem. Int. Ed. Engl.* **2022**, *61*, 202107076; b) X. Ai, Z. Wang, H. Cheong, Y. Wang, R. Zhang, J. Lin, Y. Zheng, M. Gao, B. Xing, *Nat. Commun.* **2019**, *10*, 1087; c) L. Lin, L. V. Wang, *Nat. Rev. Clin. Oncol.* **2022**, *19*, 365.
[30] J. Yuan, Y. Zhang, L. Zhou, G. Zhang, H.-L. Yip, T.-K. Lau, X. Lu, C. Zhu, H. Peng, P. A. Johnson, M. Leclerc, Y. Cao, J. Ulanski, Y. Li, Y. Zou, *Joule* **2019**, *3*, 1140.
[31] Y. Tsuchiya, K. Tsuji, K. Inada, F. Bencheikh, Y. Geng, H. S. Kwak, T. J. L. Mustard, M. D. Halls, H. Nakanotani, C. Adachi, *Front. Chem.* **2020**, *8*, 403.
[32] G. Feng, G.-Q. Zhang, D. Ding, *Chem. Soc. Rev.* **2020**, *49*, 8179.
[33] a) X. Zhao, F. Zhang, Z. Lei, *Chem. Sci.* **2022**, *13*, 11280; b) X. Wan, C. Li, M. Zhang, Y. Chen, *Chem. Soc. Rev.* **2020**, *49*, 2828.
[34] F. Liu, G. L. Espejo, S. Qiu, M. M. Oliva, J. Pina, J. S. Seixas de Melo, J. Casado, X. Zhu, *J. Am. Chem. Soc.* **2015**, *137*, 10357.
[35] a) G. Niu, X. Bi, Y. Kang, H. Zhao, R. Li, M. Ding, B. Zhou, Y. Zhai, X. Ji, Y. Chen, *Adv. Mater.* **2024**, *36*, 2407199; b) N. Yu, J. Zhou, M. Ding, M. Li, S. Peng, J. Li, *Angew. Chem., Int. Ed. Engl.* **2024**, *63*, 202405639.
[36] M. Liu, J. Li, D. Zhao, N. Yan, H. Zhang, M. Liu, X. Tang, Y. Hu, J. Ding, N. Zhang, X. Liu, Y. Deng, Y. Song, X. Zhao, *Biomaterials* **2022**, *283*, 121415.
[37] a) E. Lamprou, S. Mourtas, M. Mantzari, A. Marazioti, F. Gkartziou, S. G. Antimisiaris, *Proceedings* **2021**, *78*, 4; b) S. M. Roy, S. Barman, P. Kishore, B. Chatterjee, P. Bag, T. Ghatak, A. Basu, S. K. Ghosh, A. Dirisala, A. K. Sarkar, A. H. Khan, S. Ghosh Dastidar, A. R. Maity, *ACS Appl. Nano Mater* **2023**, *6*, 18988.
[38] a) M. Chen, D. Liu, F. Liu, Y. Wu, X. Peng, F. Song, *J. Controlled Release* **2021**, *332*, 269; b) J. Bonet-Aleta, M. Sancho-Albero, J. Calzada-Funes, S. Irusta, P. Martin-Duque, J. L. Hueso, J. Santamaria, *J. Colloid Interface Sci.* **2022**, *617*, 704; c) T. J. van 't Erve, B. A. Wagner, K. K. Ryckman, T. J. Raife, G. R. Buettner, *Free Radic Biol. Med.* **2013**, *65*, 742.
[39] a) Y. Dong, S. Dong, C. Yu, J. Liu, S. Gai, Y. Xie, Z. Zhao, X. Qin, L. Feng, P. Yang, Y. Zhao, *Sci. Adv.* **2023**, *9*, adi9980; b) J. Zhuang, Z. Ma, N. Li, H. Chen, L. Yang, Y. Lu, K. Guo, N. Zhao, B. Z. Tang, *Adv. Mater.* **2024**, *36*, 2309488.
[40] L. Kong, Z. Huang, P. Chen, H. Wang, S. Zhu, J. Yang, *Dyes Pigm.* **2020**, *173*, 107886.
[41] a) M. C. Ding, H. Y. Chen, C. F. Guimaraes, R. L. Reis, L. J. Wu, F. L. Zhang, Y. Q. Lv, T. Y. Wang, Q. H. Zhou, J. S. Shi, X. Y. Kong, *Adv. Funct. Mater.* **2024**, *34*, 2315551; b) B. M. Vickerman, E. M. Zywot, T. K. Tarrant, D. S. Lawrence, *Nat. Rev. Chem.* **2021**, *5*, 816; c) J. Ye, Y. Fan, Y. Kang, M. Ding, G. Niu, J. Yang, R. Li, X. Wu, P. Liu, X. Ji, *Adv. Funct. Mater.* **2024**, https://doi.org/10.1002/adfm.202416265.
[42] Y. Fan, J. Ye, Y. Kang, G. Niu, J. Shi, X. Yuan, R. Li, J. Han, X. Ji, *Sci. Adv.* **2024**, *10*, adm9561.
[43] M. Yang, C. Zhang, R. Wang, X. Wu, H. Li, J. Yoon, *Small Meth* **2023**, *7*, 2201381.
[44] a) M. He, M. Xiao, R. Wang, J. Fan, X. Peng, W. Sun, *Prog. Mater. Sci.* **2025**, *147*, 101347; b) B. Zhou, J. Liu, M. Lin, J. Zhu, W. R. Chen, *Coordin. Chem. Rev.* **2021**, *442*, 214009.
[45] A. Del Prete, V. Salvi, A. Soriani, M. Laffranchi, F. Sozio, D. Bosisio, S. Sozzani, *Cell Mol. Immunol.* **2023**, *20*, 432.
[46] J. Wan, L. Ren, X. Li, S. He, Y. Fu, P. Xu, F. Meng, S. Xian, K. Pu, H. Wang, *Proc. Natl. Acad. Sci. USA* **2023**, *120*, 2210385120.
[47] a) Y. He, L. Zhan, J. Shi, M. Xiao, R. Zuo, C. Wang, Z. Liu, W. Gong, L. Chen, Y. Luo, S. Zhang, Y. Wang, L. Chen, H. Guo, *Adv. Sci. (Weinh)* **2023**, *10*, 2207650; b) S. Sheng, X. Yu, G. Xing, L. Jin, Y. Zhang, D. Zhu, X. Dong, L. Mei, F. Lv, *Adv. Funct. Mater.* **2023**, *33*, 2212118.
[48] Z. Wang, Q. Su, W. Deng, X. Wang, H. Zhou, M. Zhang, W. Lin, J. Xiao, X. Duan, *ACS Nano* **2024**, *18*, 28038.
[49] Q. Xin, H. Ma, H. Wang, X.-D. Zhang, *Exploration* **2023**, *3*, 20220011.
[50] S. Song, Y. Zhao, M. Kang, F. Zhang, Q. Wu, N. Niu, H. Yang, H. Wen, S. Fu, X. Li, Z. Zhang, B. Z. Tang, D. Wang, *Adv. Mater.* **2024**, *36*, 2309748.
[51] K. M. Tsoi, S. A. MacParland, X. Z. Ma, V. N. Spetzler, J. Echeverri, B. Ouyang, S. M. Fadel, E. A. Sykes, N. Goldaracena, J. M. Kaths, J. B. Conneely, B. A. Alman, M. Selzner, M. A. Ostrowski, O. A. Adeyi, A. Zilman, I. D. McGilvray, W. C. Chan, *Nat. Mater.* **2016**, *15*, 1212.
[52] M. Scaranti, E. Cojocaru, S. Banerjee, U. Banerji, *Nat. Rev. Clin. Oncol.* **2020**, *17*, 349.
[53] a) R. Lima-Sousa, B. L. Melo, C. G. Alves, A. F. Moreira, A. G. Mendonça, I. J. Correia, D. de Melo-Diogo, *Adv. Funct. Mater.* **2021**, *31*, 2010777; b) S. M. Jin, Y. J. Yoo, H. S. Shin, S. Kim, S. N. Lee, C. H. Lee, H. Kim, J. E. Kim, Y. S. Bae, J. Hong, Y. W. Noh, Y. T. Lim, *Nat. Nanotechnol.* **2023**, *18*, 390.